Optimising CH$_4$ simulations from the LPJ-GUESS model v4.1 using an adaptive MCMC algorithm

Jalisha Theanutti Kallingal[1], Johan Lindström*[2], Paul Anthony Miller*[1], Janne Rinne[3], Maarit Raivonen[4], and Marko Scholze*[1]

[1]Department of Physical Geography and Ecosystem Science, Lund University, Lund, Sweden, S-223 62
[2]Centre for Mathematical Sciences, Lund University, Lund, Sweden, S-223 62
[3]Natural Resources Institute Finland, Helsinki, Finland, FI-00 790
[4]Institute for Atmospheric and Earth System Research/Physics, Faculty of Science, University of Helsinki, Finland, FI-00 014

Correspondence: Jalisha T. Kallingal (jalisha.theanutti@nateko.lu.se)

Abstract. The processes responsible for methane (CH$_4$) emissions from boreal wetlands are complex, and hence their model representation is complicated by a large number of parameters and parameter uncertainties. The arctic-enabled dynamic global vegetation model LPJ-GUESS is one such model that allows quantification and understanding of the natural wetland CH$_4$ fluxes at various scales ranging from local to regional and global, but with several uncertainties. The model contains detailed
5 descriptions of CH$_4$ production, oxidation, and transport controlled by several process parameters.

Complexities in the underlying environmental processes, warming-driven alternative paths of meteorological phenomena, and changes in hydrological and vegetation conditions highlight the need for a calibrated and optimised version of LPJ-GUESS. In this study we formulated the parameter calibration as a Bayesian problem, using knowledge of reasonable parameters values as priors. We then used an adaptive Metropolis Hastings (MH) based Markov Chain Monte Carlo (MCMC) algorithm to
10 improve predictions of CH$_4$ emission by LPJ-GUESS and to quantify uncertainties. Application of this method on uncertain parameters allows greater search of their posterior distribution, leading to a more complete characterisation of the posterior distribution with reduced risk of sample impoverishment that can occur when using other optimisation methods. For assimilation, the analysis used flux measurement data gathered during the period 2005 to 2014 from the Siikaneva wetlands in southern Finland with an estimation of measurement uncertainties. The data are used to constrain the processes behind the CH$_4$ dynamics,
15 and the posterior covariance structures are used to explain how the parameters and the processes are related. To further support the conclusions, the CH$_4$ flux and the other component fluxes associated with the flux are examined.

The results demonstrate the robustness of MCMC methods to quantitatively assess the interrelationship between objective function choices, parameter identifiability, and data support. The experiment using real observations from Siikaneva resulted in a reduction of RMSE from 0.044 $gC\,m^{-2}\,d^{-1}$ to 0.023 $gC\,m^{-2}\,d^{-1}$ along with a 93.89 % reduction in the cost function value.
20 As a part of this work, knowledge about how the CH$_4$ data can constrain the parameters and processes is derived. Though the optimisation is performed based on a single site's flux data from Siikaneva, the algorithm is useful for larger-scale multi-site studies for more robust calibration of LPJ-GUESS and similar models, and the results can highlight where model improvements are needed.

1 Introduction

CH$_4$ is the second most important long-lived greenhouse gas after carbon dioxide (CO$_2$) (Ciais et al., 2013; Kirschke et al., 2013). It has been reported that the global atmospheric CH$_4$ concentration has been growing since the pre-industrial time. In 2021 it reached a value of 1908 parts per billion (ppb), nearly 2.62 times greater than its estimated value in 1750 (Dlugokencky, 2021). This increase in the atmospheric concentration of CH$_4$ is responsible for around 16.5 % of the total effective radiative forcing (in $W\,m^{-2}$) of the well-mixed greenhouse gases (IPCC AR6: Forster et al. (2021)).

Among the biogenic sources, wetlands contribute around 19-33 % of current global terrestrial CH$_4$ emissions and are the largest and the most uncertain (Kirschke et al., 2013; Saunois et al., 2020; Bousquet et al., 2006). Wetlands occupy around 3.8 % of the Earth's land surface and are mainly located in high latitude regions. There is approximately 455 Pg of carbon stored in boreal and subarctic wetland peat/histosols. Under long-term anaerobic soil situations, this carbon will be metabolised by the anaerobic microorganisms called methanogens and will eventually be emitted back as CH$_4$ to the atmosphere (Aurela et al., 2009).

In the future, climate change may cause a positive feedback on emissions from wetlands CH$_4$ due to a warmer and wetter climate (Johansson et al., 2006; Bridgham et al., 2008). According to Zhang et al. (2017) at the end of the twenty-first century, 38-56 % of the CH$_4$ production from the wetlands would be climate change induced. It is also expected to have increased uncertainty in CH$_4$ emission from boreal wetlands (Christensen et al., 2007) partly due to expected spatio-temporal changes in wetland extent (Saunois et al., 2016). Considering the fragility of boreal wetlands in a changing environment (Jacob et al., 2007), one way to quantify their carbon budget is to model their carbon dynamics, including CH$_4$ emission. Realistic and optimised process-based vegetation models can be used to reach a more precise estimation of emission variability and trends. However, representation of the complex biogeochemical processes, including soil carbon turnover, vegetation dynamics, hydrology, soil thermal dynamics, and defining wetland boundaries are complex, therefore, estimating the contribution from multiple pathways for CH$_4$ production, consumption, and release complicates wetlands CH$_4$ modelling (Ahti et al., 1968; Wania et al., 2010, 2013; Susiluoto et al., 2018).

The Lund-Potsdam-Jena General Ecosystem Simulator (LPJ-GUESS) (Smith et al., 2014) is one of a few available process-based dynamic global vegetation model (DGVM) that simulates local to global vegetation dynamics and soil biogeochemistry (Smith, 2001; Sitch et al., 2003). Taking the information about the climate and concentration of CO$_2$ in the atmosphere, it predicts the structural, compositional, and functional properties of the native ecosystems of major climate zones of the Earth. Considering the complexity of LPJ-GUESS with its large number of uncertain process parameters the model requires a mathematically robust framework for parameter optimisation (Wramneby et al., 2008). Data assimilation using Bayesian statistics can be seen as a way of combining observations with prior information (i.e. model process formulation and prior model parameter values) to derive posterior parameter and emission estimates (Susiluoto et al., 2018; Ghil and Malanotte-Rizzoli, 1991; Dee, 2005; Carrassi et al., 2018). The Markov Chain Monte Carlo (MCMC) (Metropolis et al., 1953b) is a powerful and convenient Bayesian framework (Tarantola, 1987) for data assimilation as it can combine prior information with observations to sample from the posterior distributions in complex models. This study has developed an Adaptive MCMC

Metropolis Hasting (AMCMC-MH) framework (Hastings, 1970b; Tarantola, 1987) with Rao-Blackwellised adaptation of the multivariate Gaussian random walk proposals (Andrieu and Thoms, 2008). The algorithm minimises the model-data misfit, i.e.,
60 a cost function, by sampling from the probability density function (PDF) of the posterior parameters. The adaptation allows the algorithm to learn the shape of the posterior, improving sampling efficiency. The main objective of this paper is to evaluate the capabilities and limitations of the AMCMC-MH framework to optimise CH_4 wetland emissions simulated by the LPJ-GUESS model by analysing the posterior parameter distributions, the parameter correlations and the processes they control.

2 Data and Methodology

65 ### 2.1 Siikaneva wetland and measurements

The Siikaneva wetland is located at $61°,49'$ N, $24°,12'$ E, at 160 m a.s.l and is the second-largest un-drained wetland complex in Southern Finland (Ahti et al., 1968; Rinne et al., 2007). This boreal wetland complex has an area of 12 km^2, including minerotrophic and ombrotrophic sites with over 6 m of peat deposition under the surface (Mathijssen et al., 2016; Aurela et al., 2007; Rinne et al., 2007). The estimated average annual total precipitation is about 707 mm. The average temperature
70 for January and July are approximately -7.2$°C$ and 17.1$°C$, respectively. The estimated mean annual temperature is around 4.2$°C$ (Korrensalo et al., 2018). The total annual CH_4 emissions from the Siikaneva wetland varies between 6.0 gCm^{-2} and 14 gCm^{-2} and net CO_2 fluxes vary between -96 gCm^{-2} and 27 gCm^{-2} (Rinne et al., 2018).

CH_4 flux data is obtained from SMEAR-II (Alekseychik et al., b). Daily measurements of incoming short-wave radiation (swr), precipitation, and air temperature collected at the wetland are used as input to the model. Since the meteorological
75 data measured directly at the Siikaneva wetland have several significant gaps, which made them unsuitable as inputs to the model, we used precipitation and temperature data collected at a nearby station called Juupajoki-Hyytiälä (open data of Finnish Meteorological Institute (FMI)), located approximately 5.5 km away from Siikaneva. The swr data collected at at the Hyytiälä weather station, situated around 6 km from Siikaneva, is obtained from SMEAR-II (Aalto et al.). Given the short distances between these sites and Siikaneva, we assumed that the meteorological variables are representative of Siikaneva. To verify the
80 assumption, we have analysed the available data from Siikaneva and the datasets collected from Juupajoki and Hyytiälä sites. The air temperature and precipitation of the Juupajoki and the Siikaneva showed a Pearson correlation of 0.998 and 0.706, respectively. The swr data collected at Hyytiälä and Siikaneva showed a correlation of 0.98. Still, there were some minor gaps in the swr data collected at Hyytiälä, which were therefore gap-filled using the available data collected at Siikaneva, which is obtained from SMEAR-II (Alekseychik et al., a), for the corresponding periods.

85 Additional inputs to the model are atmospheric CO_2 concentration as described by McGuire et al. (2001) and updated until recent years using data from the NOAA Global Monitoring Laboratory. Daily water table depth (wtd) and soil temperature at 5 cm depth collected at the Siikaneva site are obtained from SMEAR-II (Alekseychik et al., a), and are used for evaluating the modelled values.

2.2 CH$_4$ model description in LPJ-GUESS

Compared to version 4 of LPJ-GUESS described by Smith et al. (2014), version 4.1, which we used for this study, has more detailed representations of plant functional types (PFTs) characteristics and processes in wetlands. This includes improved descriptions of peatland-specific PFTs, peatland hydrology, soil temperature estimation, and CH$_4$ emissions. Brief descriptions of the important wetland processes in LPJ-GUESS version 4.1 are given below and in Supplement Sect. S1. For a more detailed description, see Gustafson (2022).

The active wetlands peat in the LPJ-GUESS is represented by a 1.5 *m* deep column further divided into 15 layers of 0.1 *m* thickness each (see Fig. 1). The uppermost three layers comprise the acrotelm, within which the water table can vary. The underlying 12 layers of catotelm are saturated with water permanently (Wania et al., 2009a). The decomposed organic carbon in each day (explained in Sect. S1.4 in the Supplement) is distributed vertically in different peat soil layers weighted by an assumed static root distribution, see Eq. 1. This carbon pool is considered as 'potential carbon pool' for methanogenic archaea, and is the basic concept behind the CH$_4$ model in LPJ-GUESS. The total available carbon is decomposed into two components, CO$_2$ and CH$_4$ depending on the availability of O$_2$ in the soil. The dissolved CH$_4$ concentration and the gaseous CH$_4$ fraction are calculated based on the estimated CH$_4$ content in each layer. A portion of the estimated CH$_4$ is oxidised by the soil O$_2$ and the remaining is transported to the atmosphere by either diffusion, ebullition, or plant-mediated transport. Apart from being the key factor in estimating the 'potential carbon pool', root biomass in each soil layer also plays a role in the transport of O$_2$ and CH$_4$ into and out of each layer as this transport is mediated by the plants. From different studies of various wetland PFTs, Wania et al. (2010) observed an exponential decrease of root biomass with depth proportional to the degree of anoxia, which is expressed by the following equation, also used in LPJ-GUESS;

$$f_{root} = C_{root} e^{z/\lambda_{root}} \tag{1}$$

where f_{root} is the fraction of root biomass at a certain depth z, $\lambda_{\text{root}} = 0.2517$ *m* is the decay length and $C_{root} = 0.025$ is a normalisation constant. This distribution ensures that approximately 60 % of the roots are distributed within the acrotelm, and the root fraction in the lowest soil layer is adjusted to achieve a total root distribution of 1 across all 15 soil layers.

2.2.1 CH$_4$ production

Due to its wide ranges, the CH$_4$/CO$_2$ ratio from decomposition is a challenging task to predict. For example, Segers (1998) observed a high variation in the molar ratio of CH$_4$ to CO$_2$ production between 0.001 to 1.7 in anaerobic conditions. Hence it is taken in the model as an adjustable parameter weighted by the degree of anoxia α, determined as $\alpha = 1-(F_{air}+f_{air})$, where F_{air} is the fraction of air in the soil layers and f_{air} is the fraction of air in peat (Wania et al., 2009a) (see Sect. S1 in Supplement for details).
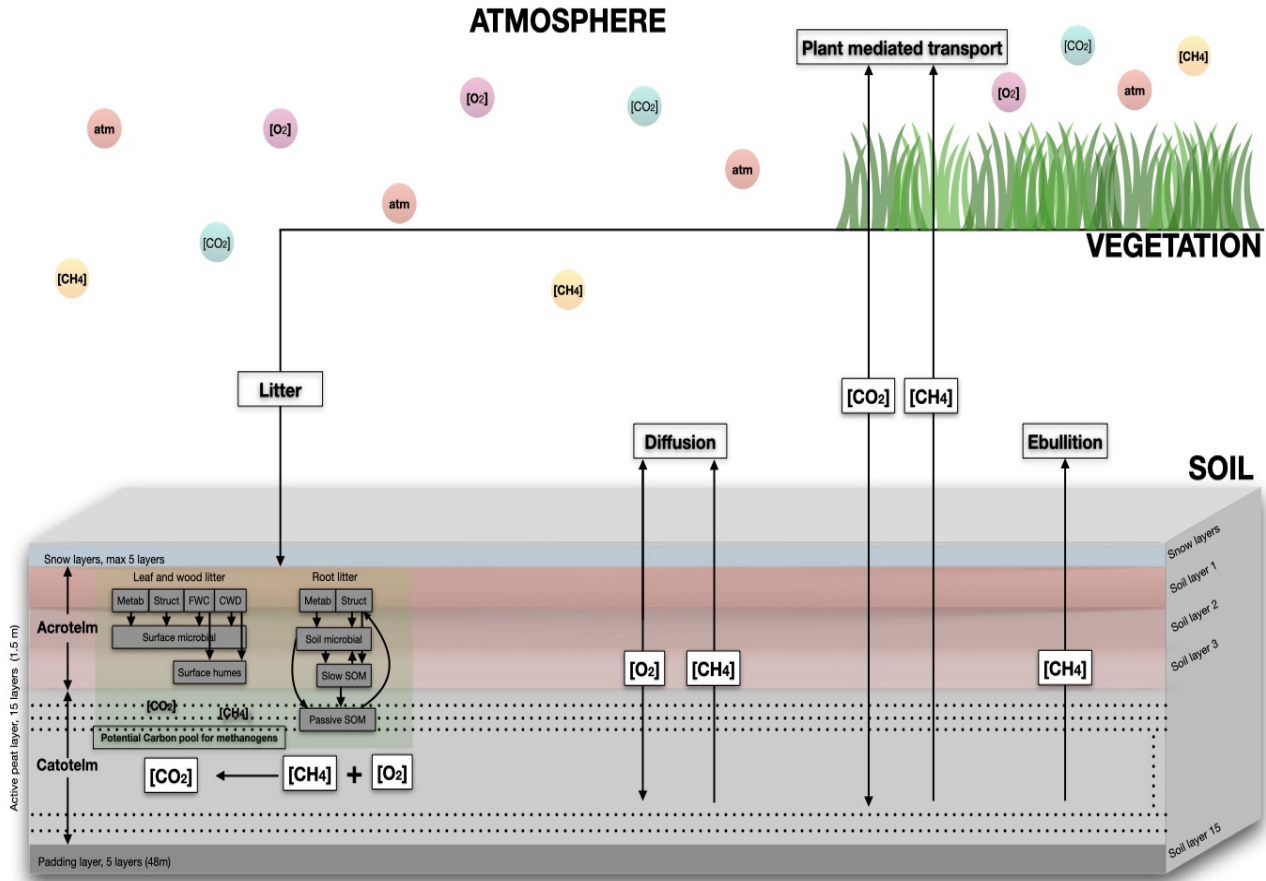
Figure 1. Schematic representation of the CH_4 model in LPJ-GUESS coupled with the CENTURY soil organic model. Carbon for methanogens is allocated to soil layers based on the distribution of roots in each layer. The root density decreases from top to bottom of peat. The assigned carbon in each layer is divided into CH_4 and CO_2. Oxygen (O_2) either directly diffuses or is transported through plants. The availability of O_2 determines the amount of CH_4 in the soil as it oxidises a fraction of CH_4. Similarly, CH_4 also can either directly diffuse or be transported to the atmosphere in bubbles, or it can be transported by vascular plants. The equilibrium between gaseous bubbles of CH_4 and dissolved CH_4 in water is controlled by the maximum solubility of CH_4. Any CH_4 that exists in gaseous form will escape to the atmosphere via ebullition.

The production of CH_4 in each day in each layer is determined as,

$$CH_{4prod} = \alpha(z) \times f_{root}(z) \times CH_4/CO_2 \times R_h \tag{2}$$

where $\alpha(z)$ is the degree of anoxia at depth z, $f_{root}(z)$ is the fraction of root in the peat at depth z, $CH_4/CO_2 = 0.085$ (prior value in the model), is the tuning parameter for the CH_4 to CO_2 production ratio, and R_h is the daily heterotrophic respiration.

Note that the model is set to $CH_{4prod} = 0$ when $F_{water} < 0.1$, assuring zero CH_4 production in frozen and/or dry soils, i.e., the model assumes there is no water when the water is frozen, hence F_{water} is 0.

2.2.2 CH₄ oxidation

As mentioned above, the CH_4 fraction that is oxidised (represented by the parameter $f_{oxid} = 0.5$ as the prior value in the model) depends on the availability of O_2 in the soil. A part of the O_2 transported to the soil will be consumed by the plant roots and non-methanotrophic microorganisms. The remaining part is then used to oxidise CH_4. The oxidised CH_4 is added to the CO_2 pool, and the remaining stays in the CH_4 pool.

2.2.3 Total CH₄ flux

Diffusion, ebullition and plant-mediated transport are the three pathways through which CH_4 is transported to the atmosphere. The total CH_4 flux from high-latitude wetland patches in the model is represented as,

$$F_{CH_4} = CH_{4diff} + CH_{4plant} + CH_{4ebul} \tag{3}$$

where CH_{4diff} is the CH_4 flux component from diffusion, CH_{4plant} is the CH_4 flux component from plant-mediated transport and CH_{4ebul} is the CH_4 flux component from ebullition. Since the daily CH_4 production in each layer is dependent on R_h (Eq. 2), F_{CH_4} is subtracted from R_h before saving the daily heterotrophic respiration. Any CO_2 generated, whether from heterotrophic respiration or CH_4 oxidation, is released into the atmosphere.

Diffusion

The fractions of CH_4, CO_2 and O_2 that are transported to the atmosphere and from the atmosphere through diffusion are calculated by solving the gas diffusion equation within the peat layers using a Crank-Nicolson numerical scheme with a time step of 15 minutes. The molecular diffusivities of these gases in soil depend on temperature, soil porosity and the water and air contents in the soil. Diffusivity in water is derived by fitting a quadratic curve to observed diffusivities at different temperatures as described in Broecker and Peng (1974); diffusivity in the air and its temperature dependency is derived from the values taken from Lerman et al. (1979), and diffusivity in soil and its temperature dependency is estimated from the Millington and Quirk model described in Millington and Quirk (1961). A detailed description can be found in Wania et al. (2010).

At the water-air surface the gas diffusivities change by minimum four orders of magnitude, hence at the water-air boundary, the flux is calculated by the following equation,

$$J = -\psi(C_{surf} - C_{eq}) \tag{4}$$

where C_{surf} is the surface water gas concentration, and C_{eq} is the concentration of gas in equilibrium with the atmospheric partial pressure, estimated using Henry's law. ψ, the gas exchange coefficient, also called piston velocity, is usually difficult to

estimate for different gases. In this case, the piston velocities of CH_4, CO_2 and O_2 are calculated by relating them to the known piston velocity of SF_6 by the following equation,

$$\psi* = \psi_{600}(\frac{Sc*}{600})^n \tag{5}$$

where $\psi_{600} = 2.07 + 0.215 \times U_{10}^{1.7}$ is the piston velocity of SF_6 normalised to a Schmidt number of 600 (subjected to the wind speed U_{10} at 10 m from the ground, which is considered as zero in the model), Sc* represents the Schmidt number of the gas under consideration, and n = - 1/2, see Wania et al. (2010) for details.

As mentioned above the diffusion through the soil is affected by soil porosity, hence by the value of $F_{air}(t, z)$. When F_{air} ≤ 0.05 in a given soil layer, the diffusivity values of water are used otherwise ($F_{air} > 0.05$) the diffusivity values of air, which are four orders of magnitude larger than those of water, are used. At each daily time step, before diffusion is calculated, the gas flux J at the boundary is used to update the dissolved gas content. The surface concentration C_{surf} of CH_4 will mostly be greater than C_{eq}; hence J will be negative, denoting a flux to the atmosphere, though it is possible for CH_4 to diffuse into the soil in small amounts if the concentrations at the surface are suitable. The resulting daily flux of CH_4 is determined as the total CH_{4diff}.

Ebullition

Ebullition depends on the solubility of CH_4 at a given temperature and pressure and occurs when the water table reaches the surface during periods of high CH_4 emission. Following Wania et al. (2010), in LPJ-GUESS, the best-fitted curve is represented as;

$$S_B = 0.05708 - 0.001545T + 0.00002069T^2 \tag{6}$$

where S_B is the Bunsen solubility coefficient, i.e. the volume of gas dissolved per volume of liquid at atmospheric pressure and a given temperature.

The CH_4 in each layer is converted to a maximum allowable dissolved mass, and this limit is used to separate the CH_4 in the form of dissolved and gaseous components. If there is any CH_4 that exceeds the maximum solubility of a layer, it will be released into the atmosphere. The CH_{4ebul} is calculated by adding this ebullition fluxes from all layers.

Plant-mediated transport

Plant-mediated transport of CH_4 occurs via the aerenchyma (the gas-filled tissues) of vascular plants either through concentration gradient or active pumping from soil to the atmosphere. Only the passive mechanism (through concentration gradient) is considered in the model as it is the most dominant one (Cronk and Fennessy, 2016). Abundance, biomass, phenology and the rooting depth of aerenchymatous plants are considered to calculate this. Only the flood-tolerant C_3 graminoids are considered for plant-mediated gas transport in the model (see Table S2 in Supplement); hence plant-mediated transport of O_2 and CH_4 can only occur when C_3 graminoids are present in a simulated patch.

The transport depends on the cross-sectional area of plant tillers (all the secondary shoots produced by grasses like *Poaceae* or *Gramineae*) in each soil layer, assuming that a significantly high percentage of CH_4 is oxidised in the highly oxic zone near the roots, where methanotrophs flourish, before they enter into the plant tissue.

The mass of the tiller is calculated as,

$$m_{tiller} = b_{graminoid} \times P(leaf) \tag{7}$$

where $b_{graminoid}$ is the leaf biomass of graminoids, and 'P' represents the daily phenology, which is the fraction of potential leaf cover that has reached full development. To calculate number of tillers (n_{tiller}) total weight of tillers, m_{tiller}, is divided by the average weight of an individual tiller (w_{tiller}). The cross-sectional area of tillers, A_{tiller} then can be obtained by,

$$A_{tiller} = n_{tiller} \times \phi_{tiller} \times \pi r_{tiller}^2 \tag{8}$$

where r_{tiller} is the tiller radius and ϕ_{tiller} is the tiller porosity. Based on the optimisation of McGuire et al. (2012), Tang et al. (2015) and Zhang et al. (2013) the value of r_{tiller} is estimated as 0.0035 *m*, and based on Wania et al. (2010) the values of ϕ_{tiller} and W_{tiller} are estimated as 70 % and 0.22 *gC/tiller* respectively. Each soil layer is allocated a fraction of the total cross-sectional area of tillers based on the root fraction estimated in that layer. The CH_{4plant} is estimated by adding the plant-mediated CH_4 fluxes from all layers.

2.3 Parameters selected for optimisation

Parameter values related to the processes of CH_4 emission in LPJ-GUESS are mostly adopted from the parameter values described in Wania et al. (2010). Since Wania et al. (2010) had difficulties finding the optimal parameter values for many of the parameters, they performed some preliminary analysis for seven uncertain parameters, for which there were little or no data available. They performed a simple initial sensitivity test by taking four sets of values for each of the seven parameters, followed by a parameter fitting exercise with three sets of values for every seven parameters. They ran the model with all their 2187 different combinations for seven sites for one year. As a result, they got a Root-Mean-Square Error (RMSE) range between 226.4 and 18.3 (*mg* CH_4 m^{-2} d^{-1}) for the different sites, which clearly indicates loosely fitted parameters with a high degree of uncertainty.

In this study, parameters for the optimisation are selected based on their sensitivity to the model output (CH_4) and expert opinion. We used a simple method to calculate the percentage difference in output (single simulation) when varying only one input parameter at a time from its permitted minimum value to its maximum (Hoffman and Miller, 1983; Bauer and Hamby, 1991). The 'sensitivity index' (SI) is calculated using the equation,

$$SI = \frac{D_{max} - D_{min}}{D_{max}} \tag{9}$$
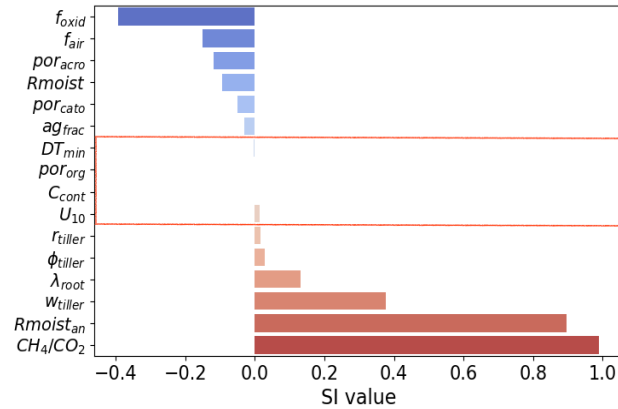
Figure 2. Tested parameters for the optimisation and their SI values. The red and blue colours indicate the increase and decrease in total CH$_4$ flux, respectively, when the value of the parameter increases.

where D_{min} and D_{max} represent the model output values corresponding to the minima and maxima of the corresponding parameter range. The values are taken based on expert opinion.

We considered five of the seven parameters Wania et al. (2010) tested in their sensitivity analysis (two parameters related to the root exudate decomposition are not used in LPJ-GUESS) together with eleven other parameters used in LPJ-GUESS. Based on their high SI values we chose eleven of them for the optimisation (Fig. 2, Table 1).

Among the five eliminated parameters. ag_{frac} is the fraction of annual net primary production (ANPP) used to calculate number of tillers; DT_{min} is the minimum temperature (°C) for heterotrophic decomposition; por_{org} is the porosity of organic material; C_{con} is the carbon content of biomass; and U_{10} is the possible constant value of wind speed at 10 m height. Among the selected parameters, $Rmoist$ and $Rmoist_{an}$, the response of soil moisture content to the soil organic matter decomposition in acrotelm and catotelm respectively (see Eq. 8 in Supplement); CH$_4$/CO$_2$, the CH$_4$ to CO$_2$ ratio in the anaerobic conditions (Eq. 2); f_{air}, the fraction of air in peat (Sect. 2.2.1 and Eq. 2); por_{acro} and por_{cato}, the porosity in acrotelm and catotelm respectively (see Sect. S1 in Supplement); and λ_{root}, the decay length of root biomass in peat (Eq. 1) are the parameters related to the CH$_4$ production. The parameter f_{oxid}, fraction of oxidised CH$_4$, (Sect. 2.2.2) is related to the CH$_4$ oxidation. w_{tiller}, the average weight of an individual tiller; r_{tiller}, the tiller radius; and ϕ_{tiller}, the tiller porosity (Eq. 8), are the parameters related to the CH$_4$ transportation.

Table 1. Selected model parameters for the assimilation. Prior values, units, prior standard deviation (*std*), and parameter description are given.

Number	Parameter	Prior value	Prior *std*	Unit	Description
1.	$Rmoist$	0.4	0.396	-	Moisture response in acrotelm
2.	CH_4/CO_2	0.085	0.236	-	Anaerobic CH_4 to CO_2 ratio
3.	f_{oxid}	0.5	0.36	-	Fraction of oxidised CH_4
4.	ϕ_{tiller}	70	36	%	Tiller porosity
5.	r_{tiller}	0.0035	0.004	m	Tiller radius
6.	f_{air}	0	4	%	Fraction of air in peat
7.	por_{acro}	0.98	0.06	-	Porosity in acrotelm
8.	por_{cato}	0.92	0.076	-	Porosity in catotelm
9.	$Rmoist_{an}$	0.025	0.04	-	Moisture response in catotelm
10.	w_{tiller}	0.22	0.24	gC	Tiller weight
11.	λ_{root}	25.17	12	cm	Decay length of root biomass

2.4 Parameter optimisation framework

We assumed Gaussian PDFs to depict both the prior distributions of the parameters and the deviation between model and observations. The resulting model can be formulated as,

$$Y|x \sim N(M(x), R),$$
$$x \sim N(x_p, B), \tag{10}$$

where Y are the observations, $M(x)$ is the LPJ-GUESS output given parameters x, x_p are the prior values of the parameters, and R and B are error covariance matrices describing the uncertainty in observations and priors, respectively.

The prior uncertainties, B, are based on expert opinion and were kept relatively large to reduce the prior's influence on the posterior parameter estimates. We have assumed prior variance for each parameters as 40 % of their expected range, see Table 1. The parameters are also assumed to be a prior uncorrelated, due to lack of good and consistent expert opinions regarding dependence.

2.4.1 Cost Function

Using the Bayesian framework the posterior for the parameters becomes

$$P(x|Y) = \frac{P(Y|x)p(x)}{p(Y)} \propto P(Y|x)p(x), \tag{11}$$

which in log-scale results in the quadratic cost function as Tarantola (1987)

$$\log P(x|Y) = -J(x) + \text{const.}$$

$$J(x) = \frac{1}{2}(Y - M(x))^t R^{-1}(Y - M(x)) + \frac{1}{2}(x - x_p)^t B^{-1}(x - x_p) \tag{12}$$

where const. represents normalising constants not depending on the unknown parameters. The two terms in $J(x)$ represent data-model misfit and the prior information on the parameters. A number of experiments aim to achieve the smallest cost function values to locate the optimal parameter set within the parameter space.

2.5 Adaptive Metropolis-Hastings

To search for the optimal posterior parameters, we used a MCMC-MH algorithm (Metropolis et al., 1953a; Hastings, 1970a). A standard Metropolis-Hastings (MH) generates samples from a target distribution by, in each iteration, drawing from a proposal distribution and then either accepting the new state or copying the old state. For a Gaussian random walk proposals, $\widehat{x}$, are generated by adding a mean-zero normal random variable to the current value, x_t:

$$\widehat{x} = x_t + \epsilon, \qquad\qquad\qquad \epsilon \sim N(0, \lambda\Sigma), \tag{13}$$

here $\lambda\Sigma$ is a scaling and covariance matrix describing the spread of the added random variable. The new value is accepted with a probability that compares the likelihood (or cost function) of the proposed and old sample,

$$\alpha = \min\left(1, \frac{P(\widehat{x}|Y)}{P(x_t|Y)}\right) = \min\left(1, \exp(-J(\widehat{x}) + J(x_t))\right) \tag{14}$$

If the value is accepted, set $x_{t+1} = \widehat{x}$, otherwise keep the previous value, $x_{t+1} = x_t$. The resulting sequence of states will represent dependent samples from the target distribution.

The Adaptive Metropolis algorithm used here contains three key concepts explained in the following sections. Transformed proposals, providing a natural way of including limits on the parameters; the adaptive random walk, allowing the algorithm to estimate λ and Σ from the target distribution; and tempering of the target distribution, to reduce the effects of local maxima and allowing better exploration of the target.

2.5.1 Transformed proposals

The standard proposal in Eq. 13 does not include any restrictions on the parameters. To handle parameter limits we transformed the parameters, resulting in an adjusted random walk proposal

$$z_t = g^{-1}(x_t),$$
$$\widehat{z} = z_t + \epsilon, \qquad \epsilon \sim N(0, \lambda\Sigma), \tag{15}$$
$$\widehat{x} = g(\widehat{z}),$$

where a list of possible limits and corresponding functions are given in Table 2. Note that different functions can be applied to each parameter in x.

Table 2. Summary of transformations and corresponding adjustments to the acceptance probability for the three cases of variables with low-limit, upper-limit, and variables constrained to an interval.

Constrain	Functions		Acceptance
	$g(x)$	$g^{-1}(x)$	$q\left(x_t \mid \widehat{x}\right)/q\left(\widehat{x} \mid x_t\right)$
$x > a$	$\exp(x) + a$	$\log(x - a)$	$\frac{\widehat{x} - a}{x_t - a}$
$x < a$	$a - \exp(x)$	$\log(a - x)$	$\frac{a - \widehat{x}}{a - x_t}$
$x \in [a, b]$	$\frac{b\exp(x) + a}{\exp(x) + 1}$	$\log\left(\frac{x-a}{b-x}\right)$	$\frac{(\widehat{x}-a)(b-\widehat{x})}{(x_t-a)(b-x_t)}$

265 Having a transformed proposal requires an adjustment of the acceptance probability (Hastings, 1970a) in Eq. 14 to

$$
\alpha = \min\left(1, \frac{p(\widehat{x}|Y)}{p(x_t|Y)} \prod_i \frac{q\left(x_t^{(i)} \mid \widehat{x}^{(i)}\right)}{q\left(\widehat{x}^{(i)} \mid x_t^{(i)}\right)}\right) =
$$
$$
= \min\left(1, \exp(-J(\widehat{x}) + J(x_t) + \sum_i \log\left(\frac{q\left(x_t^{(i)} \mid \widehat{x}^{(i)}\right)}{q\left(\widehat{x}^{(i)} \mid x_t^{(i)}\right)}\right)\right).
$$

(16)

Here $x_t^{(i)}$ denotes the ith parameter in the x_t-vector and the q-terms are given in Table 2. Note that each transformation results in one adjustment for that parameter and that all adjustments have to be multiplied together.

2.5.2 Adaptive random walk

270 It has been shown that optimal behaviour of the MH-algorithm is obtained when about 20 % to 30 % of samples are accepted (Gelman et al., 1996; Roberts et al., 1997). For the proposal in Eq. 13, this is achieved when Σ corresponds to the posterior covariance matrix of the target distribution, $P(x|Y)$, and the scaling is $\lambda = 2.38^2/d$, where d is the number of parameters in x. The key idea of the adaptive algorithms suggested in Andrieu and Thoms (2008) is to recursively estimate both Σ and λ from previous samples. An important note for the transformed proposal in Eq. 15 is that Σ and λ relate to the transformed variable 275 z_t and not x_t.

A Rao-Blackwellised update of the covariance matrix will consider both the proposal, $\widehat{z}$, and the previous value, z_t, weighted according to the acceptance probability, α, computed in Eq. 16. The expectation and covariance matrix are updated recursively as,

$$
\mu_{t+1} = (1 - \gamma_{t+1})\mu_t + \gamma_{t+1}\left(\alpha\widehat{z} + (1-\alpha)z_t\right),
$$

(17a)

$$
\Sigma_{t+1} = (1 - \gamma_{t+1})\Sigma_t + \gamma_{t+1}\left[\alpha\left(\widehat{z} - \mu_{t+1}\right)\left(\widehat{z} - \mu_{t+1}\right)^\top\right.
$$
$$
\left. + (1-\alpha)\left(z_t - \mu_{t+1}\right)\left(z_t - \mu_{t+1}\right)^\top\right],
$$

(17b)

where γ_t is an adaptation factor and we have used $\gamma_t = t^{-0.51}$.

The Global Adaptive Scaling then updates the scaling factor λ as,

$$\log \lambda_{t+1} = (1 - \gamma_{t+1}) \log \lambda_t + \gamma_{t+1} (\alpha - \alpha_{\text{target}}) . \tag{18}$$

285   The update is in log-scale to ensure that λ_t stays positive; the second part of the equation compares the current acceptance probability with a target probability, $\alpha_{\text{target}} = 0.234$, and adjust λ_t to obtain this desired overall acceptance probability.

    To limit the effect of initial values, we first ran 5 000 steps of the chain without adaptation and taking Σ as 10^{-3} times an identity matrix (i.e. very small initial steps). Thereafter, a covariance matrix Σ was estimated based on the initial samples and the chain run for a further 15 000 steps adapting only λ and not Σ. Finally, for the last 80 000 steps both λ and Σ were updated

290   as described in Andrieu and Thoms (2008). We call the resulting framework the *Global Rao-Blackwellised Adaptive Metropolis* (GRaB-AM) algorithm.

2.5.3   Tempering the target distribution

For large amounts of data, the cost function $J(x)$ can have very deep local minima causing the MH-algorithm to get stuck, even with the two already outlined adjustments. To reduce the scale of the cost function we temper the target distribution (Jennison,

295   1993).

$$\widetilde{P}(x|Y) = P(x|Y)^{1/T} = \exp(-J(x)/T), \tag{19}$$

where T is a suitably large value.

    Having run a MH-algorithm for N samples, the first N_b samples are discarded as burn-in and expectations or variances can be computed as averages of the remaining samples.

300   However, with a tempered target distribution, we have samples from $\widetilde{P}(x|Y)$ and need to use importance sampling to adjust for the difference in distributions (Jennison, 1993), resulting in weighted averages

$$E(x|Y) \approx \sum_{i=N_b}^{N} w_i x_i,$$

$$V(x|Y) \approx \sum_{i=N_b}^{N} w_i (x_i - E(x|Y))^2,$$

where the weights are given by,

305     $$w_i = \frac{\exp\left(-\frac{T-1}{T}(J(x_i) - J_{\min})\right)}{\sum_{i=N_b}^{N} \exp\left(-\frac{T-1}{T}(J(x_i) - J_{\min})\right)} .$$

and $J_{\min} = \min_i J(x_i)$. The subtraction by $J_{\min}$ is for numerical stability to avoid cases of 0/0 when all $J(x_i)$ are very large. For the case of no tempering, i.e. $T = 1$ the weights simplify to $w_i = 1/(N - N_b)$, resulting in unweighted averages.

2.6   Experiment design

We have designed a set of twin experiments and a real data experiment. For both the twin and real data experiments, we

310   generated MCMC chains with a length of 100,000 samples as mentioned in Sect. 2.5.2. MCMC approaches are computationally

intensive and time-consuming. In this study, each model simulation took approximately 9 seconds to complete (using an AMD Ryzen Threadripper processor). As a result, for the 100,000 iterations, it consumed nearly 250 computational hours. However, it should be noted that this study involves the model running for a single site, and the computational speed is highly dependent on the performance of the processors being used.

Twin experiment

315

Twin experiments are designed to assess the performance of the developed GRaB-AM and its ability to recover the parameter values. The daily CH_4 output simulated by LPJ-GUESS using randomly chosen true parameter values (Z_{true}) within their permitted range of variation are used as the synthetic observation. Since the synthesised observation conforms completely to the model, any potential errors in the model have not influenced the parameter optimisation process, ensuring unbiased posteriors.

320 The observations have been assigned uncertainties to resemble the real data experiment, as described below. It is expected that the assimilated parameters will converge to the true values as the MCMC chain progresses in time. To freely recover the Z_{true} values, the prior parameter values (x_p) in the cost function (Eq. 12) are set as Z_{true}. Two scenarios are considered for the twin experiment to test the identifiability of the parameters under different conditions. Scenario 1 with a shorter temporal scale from 2005 to 2014 (10 years); scenario 2 with a longer temporal scale from 1901 to 2015 (115 years). Scenario 1 is more realistic

325 and is chosen to mimic the real data at Siikaneva, whereas scenario 2 constitutes an ideal, hypothetical case with observations over the entire simulation period. In each set of the scenarios, the optimisation started from a different initial point in parameter space randomly selected from their prescribed ranges.

Real Data experiment

To estimate the posterior parameter values, an experiment using the real observation from Siikaneva is designed. The observed

330 daily averages are compared with the model simulation in the cost function only when more than 90 % of the hourly observation were available each day. When there are gaps in the daily observation, we eliminate them, and their corresponding modelled values from the cost function calculation. In principle the error covariance matrix R should include both observation uncertainties and their correlations. From the fact that the latter is difficult to estimate, we neglected them, and the observation uncertainties are estimated as 30 % for the daily observations greater than 0.01 $gC\ m^{-2}d^{-1}$, and a floor value of 0.3 for the

335 observations less than 0.01 $gC\ m^{-2}d^{-1}$.

2.7 Parameter value estimation

For all the experiments conducted in this study, the first 75 % of the GRaB-AM chains are discarded as the 'burn-in'. The PDFs generated after the 'burn-in' are used to estimate each parameter's maximum a posteriori probability (MAP), posterior mean and standard deviation (*std*). Following the idea used in Braswell et al. (2005) the parameter distributions are grouped

340 into three categories: 'well-constrained', 'poorly constrained', and 'edge-hitting' parameters. The well-constrained parameters are the ones that exhibit a well-defined uni-modal distribution, with low *std*. The poorly constrained parameters are the ones that exhibit a relatively flat multi-modal distribution with large *std*. To be more precise with the estimation, for the posterior

parameter distributions appeared multi-model if the *std* of the distribution is greater than 20 % of its total range, we classified them as poorly constrained. The edge-hitting parameters are the ones that cluster near one of the edges of their prior range.

2.8 Posterior re-sampling experiment

To examine the effect of parameter optimisation on flux components, we designed a re-sampling experiment from the posterior parameter distributions. From the experiment conducted using site observation, 1000 sets of parameters are randomly selected and used to run the model to simulate the CH_4 flux components. The outputs from each simulation of the experiment are used to analyse the process correlations and process-parameter relationships.

3 Results

3.1 Twin experiment using GRaB-AM

We ran a set of four different twin experiments for each scenarios mentioned in Sect. 2.6. Each of them shows a reasonably good convergence, regardless of their chosen initial values. In scenario 1, all parameters except for CH_4/CO_2 and λ_{root} showed good convergence (see Fig. S1 in the Supplement, posterior parameter correlations of the first experiment shown in Fig. S1 are provided in Fig. S2 of the Supplement). The results of scenario 2 are not shown, as they followed the same pattern. The resulting PDFs of experiment 1 in scenario 1 after the 'burn-in' are represented in Fig. 3 showing the mean and MAP values as well as the *std* of the parameters. The parameter values and related statistics are given in Table 3.

The parameter retrieval capacity of the GRaB-AM algorithm is estimated as the 'retrieval score' by dividing the posterior mean estimates of the parameters from all the chains in each scenario by Z_{true} parameter values. The idea behind the retrieval score is that in an ideal case of complete recovery, the posterior parameter estimate and the Z_{true} value are the same; hence the retrieval score would be one. Figure 5 shows the retrieval scores obtained for each parameter and their 1σ value. In scenario 1 the ϕ_{tiller}, por_{acro}, por_{cato}, w_{tiller} and λ_{root} are well retrieved with a low *std*. Scenario 2 performed better in parameter retrieval compared to scenario 1. In scenario 2 the majority of the parameters except the CH_4/CO_2, r_{tiller}, w_{tiller} and λ_{root} were showing good retrieval scores, but with comparatively high *std*s (see Fig. 5). The overall mean retrieval score estimation is based on the ratio of the estimated and true values, given a value of 0.95 with a *std* of 0.19 for scenario 1, and a value of 1 with *std* 0.21 for scenario 2 (see Fig. 5).

In general, the twin experiments have resulted in 'well-constrained' and 'poorly constrained' parameter classes. Examples of the different classes of the distributions for experiment 1 of scenario 1 are shown in Fig. 3. Based on the posterior distributions estimated from all the four GRaB-AM chains the parameters $Rmoist$, CH_4/CO_2, f_{oxid}, r_{tiller}, f_{air}, por_{acro}, por_{cato} and λ_{root} are well constrained in scenario 1 and the parameters $Rmoist$, CH_4/CO_2, f_{oxid}, r_{tiller}, f_{air}, por_{acro}, por_{cato}, w_{tiller} and λ_{root} are well constrained in scenario 2 (See Table 3).

The reduced posterior cost function values and their χ^2 values are given in Table 4. Here, the reduced χ^2 values are calculated by dividing twice the cost function by the number of observations used in the assimilation. Overall, the χ^2 values indicate a
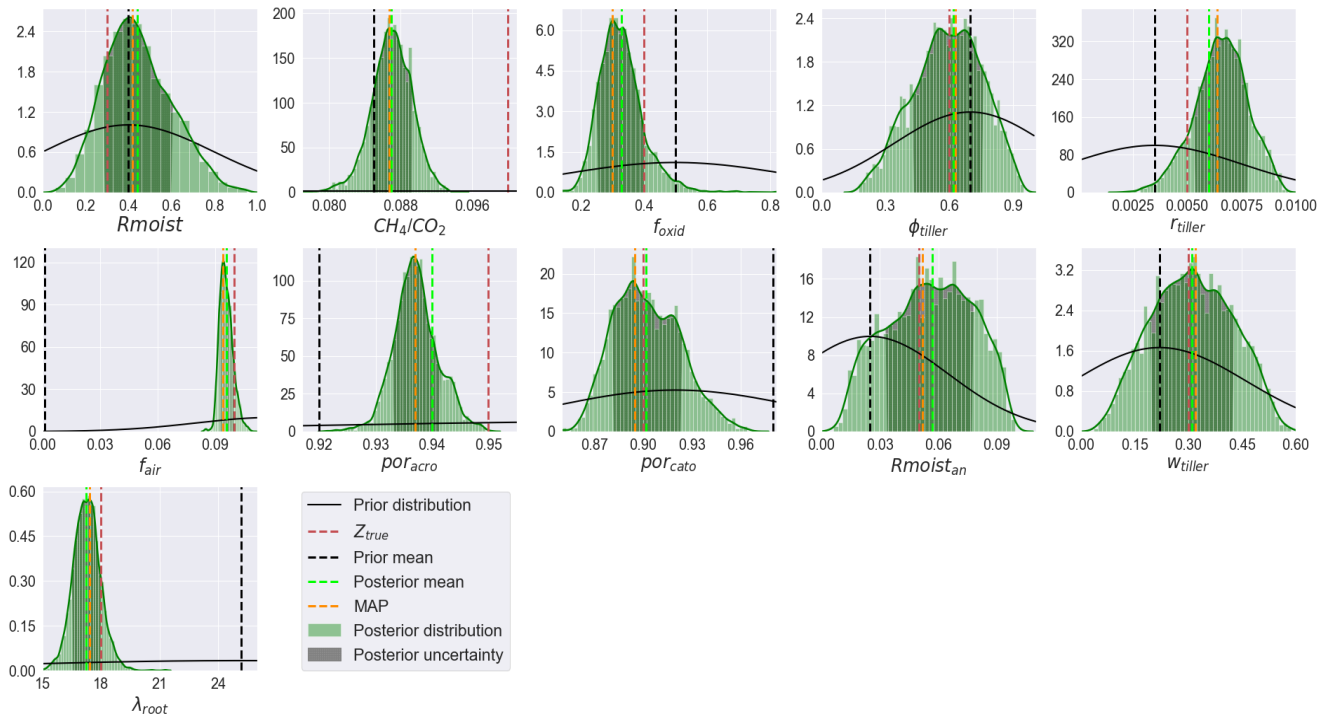
Figure 3. An example of posterior PDFs from the twin experiment. Prior and posterior distributions are illustrated with black and green solid lines respectively. True parameter values (Z_{true}), prior mean, and MAP are shown in red, black, lime and orange colors respectively.

Table 3. Posterior mean, MAP and *std* of retrieved parameters for selected twin experiments in both scenarios (Sc) and the parameter classes estimated from analysing the distributions of all four chains. The parameter classes include well-constrained (WC) and poorly-constrained (PC) parameters.

| | | Parameter | | | | | | | | | | |
		Rmoist	CH_2/CO_2	f_{oxid}	ϕ_{tiller}	r_{tiller}	f_{air}	por_{acro}	por_{cato}	$Rmoist_{an}$	w_{tiller}	λ_{root}
Sc 1	Z_{true}	0.30	0.1	0.40	0.60	0.005	0.10	0.95	0.90	0.05	0.30	18.0
	MAP	0.42	0.086	0.31	0.63	0.006	0.094	0.93	0.89	0.051	0.32	17.4
	Posterior mean	0.40	0.087	0.33	0.60	0.006	0.096	0.94	0.90	0.057	0.30	17.2
	$std\mp$	0.16	0.002	0.07	0.16	0.001	0.003	0.004	0.02	0.02	0.10	0.70
	Class	WC	WC	WC	PC	WC	WC	WC	WC	PC	PC	WC
Sc 2	Z_{true}	0.30	0.1	0.40	0.60	0.005	0.10	0.95	0.90	0.05	0.30	18.0
	MAP	0.22	0.079	0.24	0.64	0.006	0.09	0.94	0.89	0.064	0.29	13.9
	Posterior mean	0.28	0.08	0.26	0.63	0.006	0.10	0.95	0.89	0.053	0.26	14.1
	$std\mp$	0.07	0.002	0.05	0.18	0.001	0.0008	0.0009	0.006	0.01	0.01	0.42
	Class	WC	WC	WC	PC	WC	WC	WC	WC	PC	WC	WC
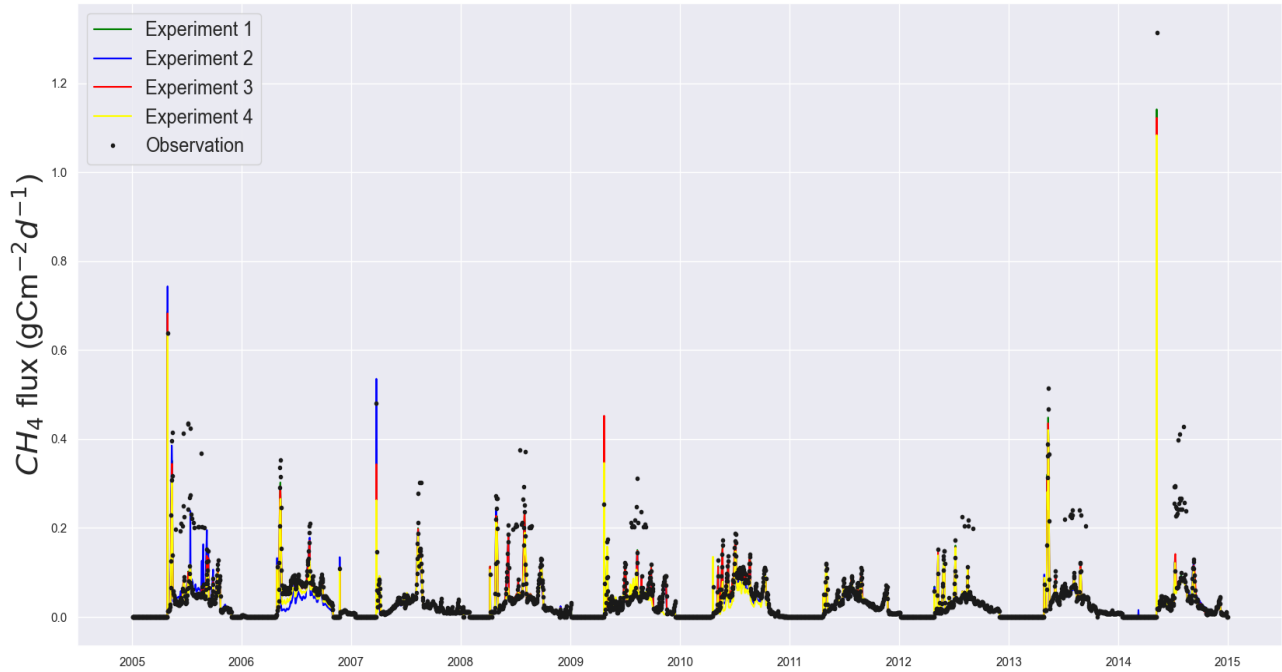
Figure 4. Time series estimates of the twin experiments in scenario 1. The simulations, using four sets of posterior parameter values obtained from the twin experiments are plotted against the twin observation used.

Table 4. Cost function reduction observed in two different scenarios (Sc) of the twin experiments. Prior and posterior cost function values obtained from four sets of experiments for each scenario are provided. The misfit between observed and expected (zero) cost function values are represented as the reduced χ^2 value.

	Experiment	Prior	Posterior	χ^2
Sc 1	Set 1	12486.4	301.6	0.17
	Set 2	49674.0	759.6	0.422
	Set 3	29535.6	294.0	0.17
	Set 4	8476.8	428.0	0.24
Sc 2	Set 1	86140.0	6170.0	0.31
	Set 2	619172.0	8040.0	0.38
	Set 3	68792.0	3372.4	0.16
	Set 4	109888.0	8646.0	0.41

statistically robust reduction in the cost function in all the experiments, although a systematic behaviour of being below one is

375 observed.
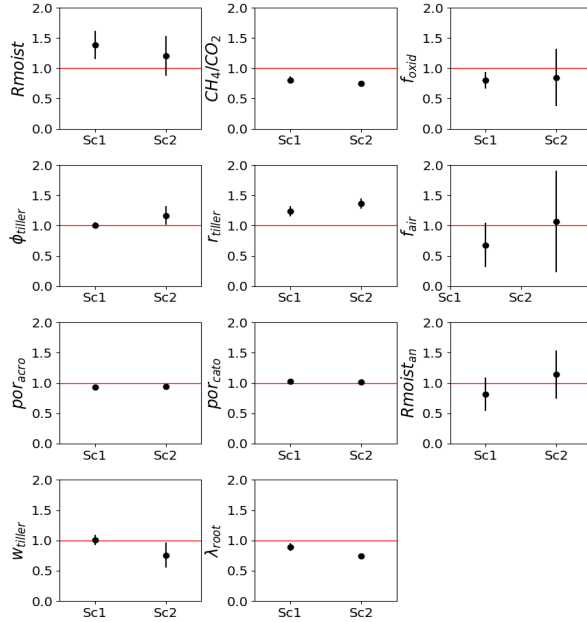
Figure 5. Twin experiment results in terms of mean 'retrieval score' based on the ratio of the estimated and Z_{true} values of the parameters. The horizontal red lines indicate a complete retrieval, and the error bar shows the *std* obtained from different chains in different scenarios. Sc1 and Sc2 indicate the two scenarios.

3.2 Real data experiments and optimised parameters

For the experiment with the real data, the observations collected at the Siikaneva wetland are assimilated using the GRaB-AM algorithm. The MCMC trace plots are exemplified in Fig. 6.

3.2.1 Optimised parameter values and distributions

380   The posterior parameter PDFs are shown in Fig. 7. In contrast to the twin experiments, the parameters fell into three categories: 'well-constrained', 'poorly constrained', and 'edge-hitting'; the classifications are given in Table 5. The PDFs for parameters $Rmoist$, CH_4/CO_2, ϕ_{tiller}, f_{air}, por_{acro}, w_{tiller} and λ_{root} are classified as well constrained distributions. The PDFs for r_{tiller}, por_{cato} and $Rmoist_{an}$ are classified as poorly constrained distributions, and the one for f_{oxid} is classified as a edge-hitting distribution. Both in the well-constrained and poorly constrained parameters, high kurtosis is observed. The values of
385   f_{oxid}, which is the edge-hitting parameter, lay near the higher bound of the edges of the prior range, and most of the retrieved values were clustered near this edge. The parameter also exhibited large positive kurtosis and negative skewness. The posterior parameter values and their 1σ *std*s along with the prior values are shown in Table 5. The MAP and posterior mean estimates agree on the value for the parameters CH_4/CO_2, f_{air} and por_{acro}. For f_{oxid}, ϕ_{tiller} and r_{tiller}, both the MAP and posterior mean estimates stayed out of 1/3 of the 1σ range of the posterior distribution, which we consider a large difference. For the
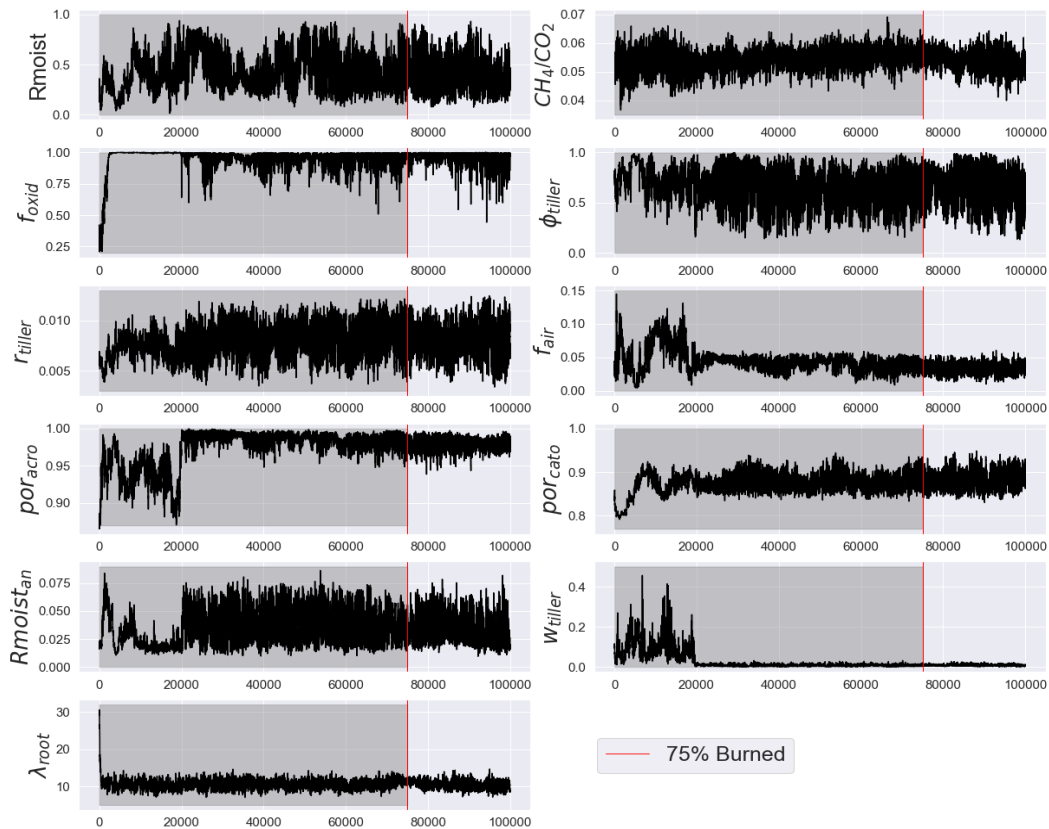
Figure 6. An example of the GRaB-AM chains for the experiment with real observations showing all the 100,000 values in the chain. The first 75 % were discarded as 'burn-in' and is greyed out in the figures. The remaining 25 % (from the red vertical lines) were used for the analyses.

390   remaining parameters, the MAP and posterior mean estimates stayed within 1/3 of the 1σ of their posterior distribution; hence we consider this as a small difference. For the parameters $Rmoist$ and CH_4/CO_2 the posterior values appeared close to, but below the prior values. The posterior values of $Rmoist_{an}$ appeared very close to, but above the prior values. For the parameter ϕ_{tiller} the MAP estimate appeared very close to but above the prior value and posterior mean estimate appeared very close to but below the prior value. For these four parameters, the posterior mean stayed within 1/3 of the 1σ range of the assumed prior

395   uncertainty. The parameters f_{oxid}, r_{tiller}, and f_{air} posterior values appeared slightly above the prior values, but out of the 1/3 of the 1σ range of the prior uncertainty. The prior and posterior values of the parameter por_{acro} remained the same. In contrast, the parameters por_{cato}, w_{tiller} and λ_{root} appeared far distant from, and below the prior values, out of 1/3 of the 1σ range of prior uncertainty, but stayed within the prior range (see Sect. 4.2 for details).

3.2.2 Posterior parameter correlation

The 2D distributions of the posterior parameters and their correlations are illustrated in Fig. 9. Overall, the majority of the parameters showed weak positive or negative correlations with a few exceptions with extreme correlations (the values and corresponding colour code in the triangle above depict this). For example, $Rmoist_{an}$ showed high negative correlation to $Rmoist$, and por_{acro} showed high positive correlation to f_{air}. The 2D marginal distributions (scatter plots), illustrated in the lower triangle, showed a general tendency of high clustering within the 1σ range for all the parameters; in general, the 1D histograms (on the diagonal, also shown in Fig. 7) appeared as well-constrained uni-modal distributions. For further details, see Sect. 4.2.1.

3.2.3 Cost function reduction

The prior and posterior cost function values corresponding to prior and posterior parameter values are listed in Table 5. The prior cost function value calculated with the default model parameters showed a high-cost value of 48424.4 with a model overestimation of around four times the observed flux. After the optimisation, the cost function value was reduced to 2959.8 (reduced $\chi^2 = 3.82$) with the MAP estimate of parameters and to 3002.6 (reduced $\chi^2 = 3.88$) with the posterior mean estimate of parameters.

3.2.4 Flux components of CH$_4$ simulation and parameter values

To understand how and how much in magnitude each optimised parameter influences the flux components and the total flux, the result of the 're-sampling experiment' (see Sect. 2.8) is examined through correlation and regression analyses. The Pearson correlation coefficients and regression slopes are calculated for all the 1000 parameter sets and their corresponding sums of the flux components and total flux. The left side of Fig. 8 shows a schematic summary of the correlation coefficients and regression slopes between the 11 parameters, the flux components and the total flux. For both the total flux and diffusion, all parameters, except f_{oxid} and ϕ_{tiller}, showed a similar regression pattern, although with slight differences in magnitudes. This similarity is not surprising as diffusion is the most dominant among the process components. The total flux showed highest correlations to CH_4/CO_2 and λ_{root} and lowest correlation to f_{oxid}. A detailed discussion of the process-parameter relations can be found in Sect. 4.2.1.

The right side of Fig. 8 shows the correlations between the sums of flux components resulted from the 're-sampling experiment'. The 2D distributions in the lower triangle show a strong positive relation between diffusion and total flux. Almost all the parameter residuals are observed within the 3σ deviation without many outliers. Except for the correlation between diffusion and total flux, the analysis showed no other strong positive or negative correlation between the components, as can be seen in the correlation plot illustrated in the top triangle.
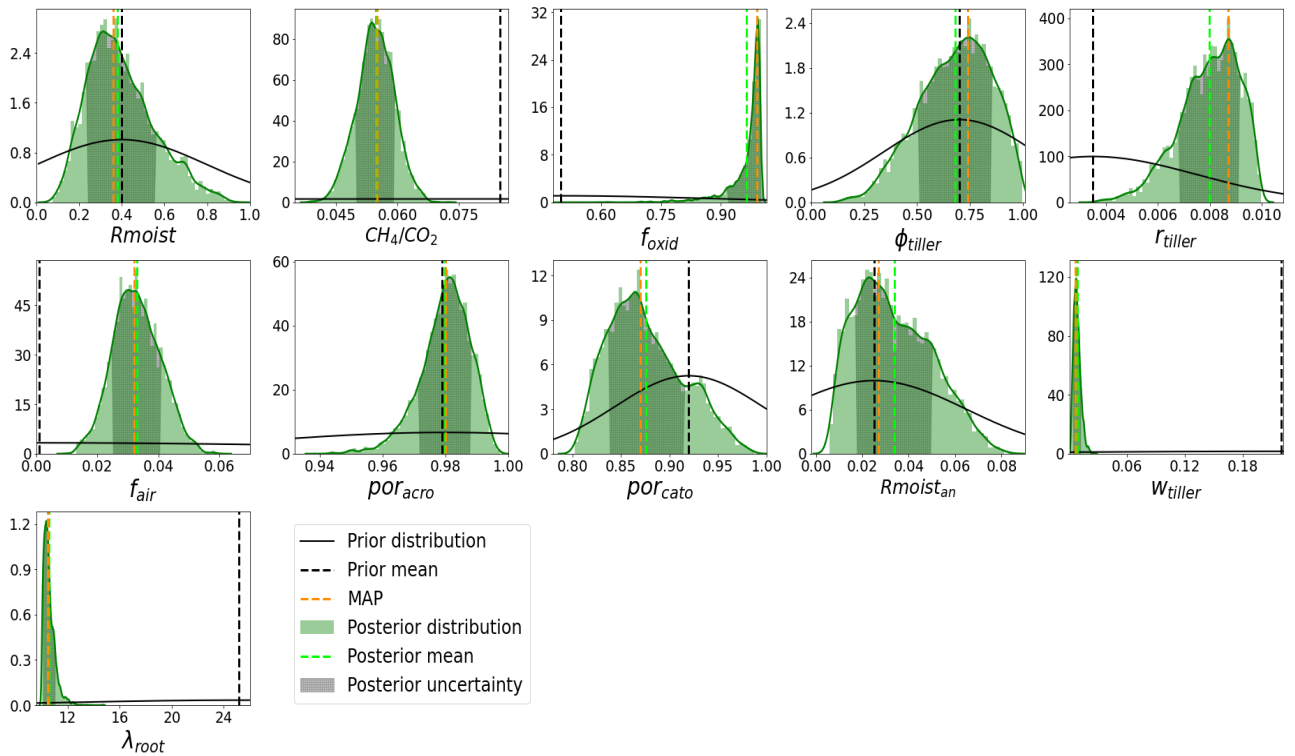
Figure 7. Posterior PDFs of parameters from GRaB-AM real data experiment. The green curves shown are the smoothed Gaussian kernel estimates of the posterior distribution on the posterior histograms, and the black curves are the prior distributions. The dotted vertical black, lime and orange lines represents the prior mean, posterior mean, and MAP, respectively. The shaded green area of the distributions represents the 1 σ error estimate of the PDFs.

Yearly variations in fractional contributions of flux components simulated using prior and posterior parameter estimates are examined to understand the impact of the optimisation on the composition of the inter-annual emissions. The time series of 430 the annual sums of flux components as a function of their total flux (in %) are shown in Fig. 10a. The result shows that among the flux components, diffusion contributes the most to the total CH_4 flux both in prior and posterior estimates, with a slightly higher contribution in the posterior estimate, followed by plant-mediated transport (see Sect. 4.2.3 for detailed discussion).

The time series model-observation mismatch of prior and posterior estimates for the annual total fluxes can be seen in Fig. 10b; the values are in percentage of the observed CH_4 flux. The prior estimate showed a mismatch of around 600 % for 435 the first two years. Also, a considerably high mismatch is observed in the years 2011, 2012 and 2014. The MAP estimate remained near zero, while the posterior mean estimate exhibited slightly negative values indicating an underestimation of the flux. Interestingly, the MAP followed the same pattern as the prior estimation by showing an increase whenever the prior increased and a decrease whenever the prior decreased; however, the posterior mean estimate did not show this relation.

Table 5. Parameter values estimated after the GRaB-AM real data optimisation. The prior values, MAP, posterior mean, posterior *std* and parameter classes are shown. The parameter classes include well-constrained (WC) and poorly-constrained (PC), and edge-hitting (EH) parameters. The cost function values correspond to the parameter values obtained with prior, MAP and posterior mean estimates are also shown.

Parameter	$Rmoist$	CH_4/CO_2	f_{oxid}	ϕ_{tiller}	r_{tiller}	f_{air}	por_{acro}	por_{cato}	$Rmoist_{an}$	w_{tiller}	λ_{root}	Cost value
Prior values	0.4	0.085	0.5	0.7	0.0035	0.0	0.98	0.92	0.025	0.22	25.17	48424
MAP	0.37	0.055	0.98	0.74	0.0087	0.032	0.98	0.87	0.029	0.0061	10.47	2959.8
Posterior mean	0.39	0.055	0.96	0.68	0.0079	0.032	0.98	0.88	0.033	0.0082	10.58	3002.6
$std \mp$	0.15	0.0046	0.046	0.17	0.0011	0.007	0.008	0.038	0.016	0.0037	0.45	
Class	WC	WC	EH	WC	PC	WC	WC	PC	PC	WC	WC	

The percentage fractions of the annual errors of the flux components are shown in Fig. 11. The effect of optimisation on the individual contributions of each component can be seen from the annual means (solid dots) of their fractional contribution to the total flux. Among the prior estimates of flux components, the prior plant-mediated transport showed the largest error (22.5 %), and the ebullition showed the smallest error (9.1 %). In the MAP estimate, ebullition showed the highest error with a value of 12.3 %, followed by diffusion and ebullition with around the same value of error, 6.9 % and 6.8 %, respectively. For the estimate using posterior mean values, diffusion and plant-mediated transport showed around the same errors, 7.5 % and 7.4 %, and the ebullition showed the least error (2.6 %). On the right-hand side of the figure, the fourth column displays the mean and errors for the inter-annual variation of the total fluxes obtained by prior parameter values and posterior estimates. The prior total estimate showed an error of 4.2 %, and the mean and MAP showed an error of 0.66 % and 0.72 %, respectively.

3.3 Fit to the observation

Figure 10b illustrates the percentage model-data misfit, and Fig. 12 shows the time series of the assimilated observations together with the model prior and posterior estimates with their uncertainties. The total RMSE estimated between the prior and observations were 0.044 $gC\ m^{-2}\ d^{-1}$, which got reduced to a value of 0.023 $gC\ m^{-2}\ d^{-1}$ for the posterior case. The result indicates that most of the mismatch between the prior model estimates and observations was contributed by the large overestimation in the initial years. This overestimation disappeared in the posterior, showing a better agreement with the observation. There are years for which the observations show large peaks during the summer (such as 2010, 2012 and 2013), and the posterior estimates succeeded in capturing these peaks to a large extent, but not completely (see Sect. 4.5 for details).
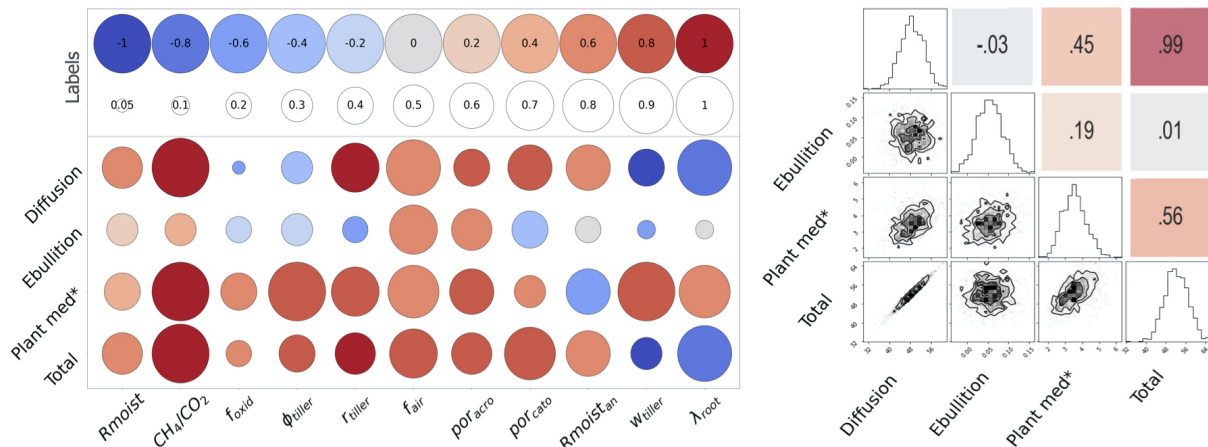
Figure 8. Schematic summery of the 're-sampling experiment'. The image on the left side shows the process-parameter correlation and regression slope. Three different flux components of CH₄ together with the total flux are labelled on the vertical axis, and the parameters are labelled on the horizontal axis. The different colours of the circles represent the regression slopes (β) scaled between -1 and 1 (in 11 steps). The blue colour indicates a steeper negative slope hence a strong decrease, and the red colour indicates steeper positive slopes hence a strong increase in CH₄ fluxes with the increasing parameter value. The coefficient of determination (R^2) scaled between 0.05 and 1 (in 11 steps) is represented by the size of the circles, with larger circles indicating higher R^2 values. The image on the right side shows the process-process correlations. Numeric labels on the upper triangle correspond to Pearsons correlation coefficient values. The diagonal of the matrix shows the 1-D histogram for each flux components and the total flux. 2-D marginal distributions of the sum of the processes and total flux are represented in the lower triangle with contours to indicate 1σ, 2σ and 3σ confidence levels. The black dots in the plots indicates the sums of flux components. Ranges of the distributions are labelled on the left and bottom of the figure.

4 Discussion

4.1 Twin experiment

A common problem with the adaptive MH algorithm is its inability to widely explore the target distribution if the set-up is not well tuned. This can then result in a poor approximation of the target distribution, hence poor adaptation. The resulting trace
460   plots shown in Fig. 6 and Supplement Fig. S1 depict a set of well-explored parameters on their permitted space ranges during the progression of the random walk, which indicates a well-tuned assimilation setup. The use of the Adaptive, Blackwellised learning of the posterior distribution appeared beneficial during the transients of the chains whenever the acceptance probability has been dropped to low values at low probability regions of the parameter space.

Even though twin experiments have retrieved all true parameters in different experiments, individual experiments reveal
465   instances where one or two parameters may not fully converge to their true values due to factors such as parameter correlation or equifinality (Fig. 5 and Supplement Fig. S1). Given the complexity and non-linearity of the model, it is not surprising that not all parameters converged completely. It is also not surprising that different chains estimated slightly different posterior
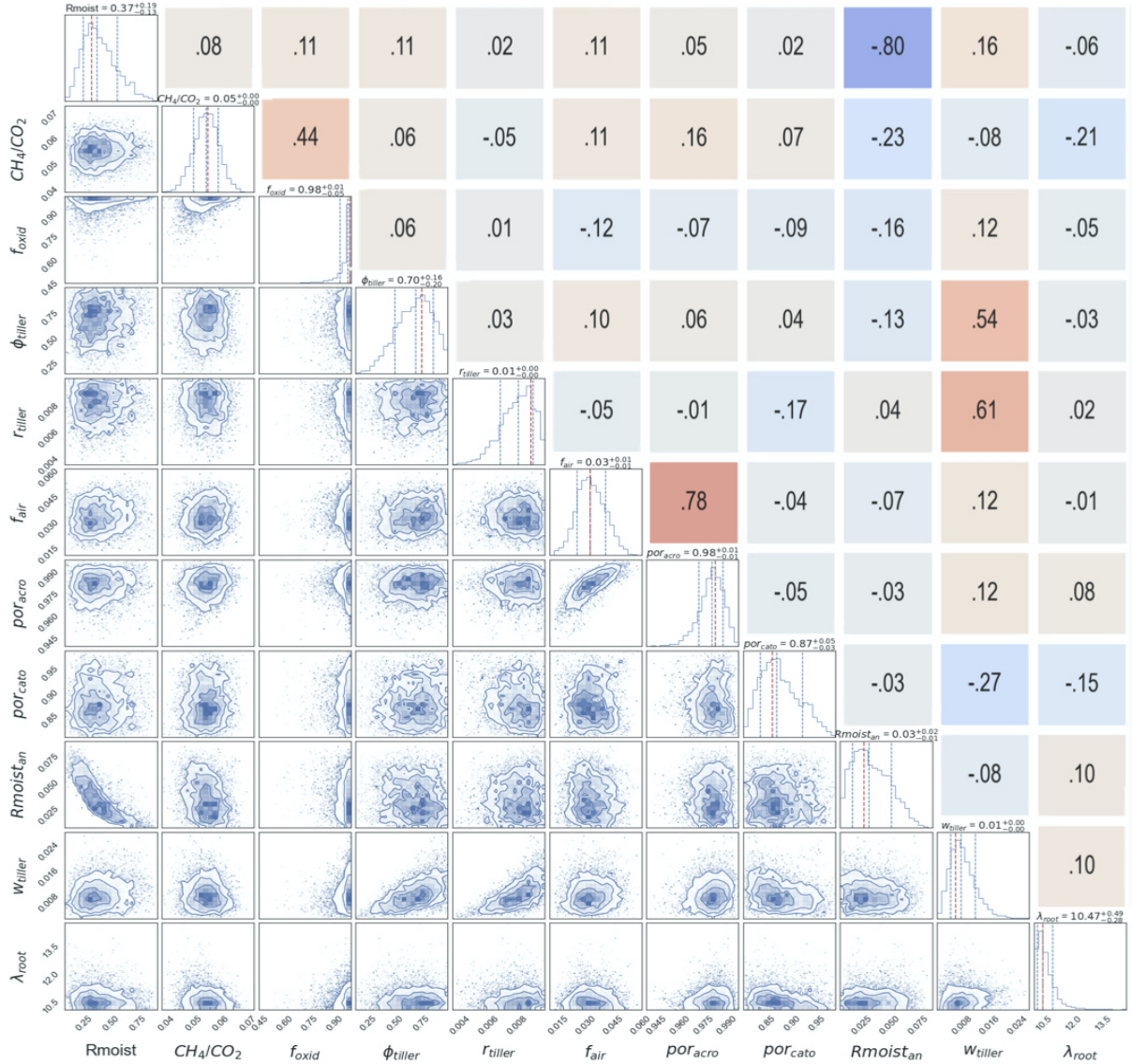
Figure 9. A posteriori correlations between the parameters from the GRaB-AM real data optimisation. The blue and red colour in the upper triangle represents the strong negative and positive correlations, respectively. The numerical labels on the upper triangle are the values of Pearson's correlation coefficient. The panels on the diagonal show the 1-D histogram for each model parameter with a dashed red vertical line to indicate the mode. The vertical blue lines are the 0.16, 0.5 and 0.84 quantiles of the distributions. The lower triangle represents the two-dimensional marginal distributions of each parameter with contours to indicate 1σ, 2σ and 3σ confidence levels, and the blue dots on the marginal distributions are the posterior parameter values. Ranges of the distributions are labelled on the left and bottom of the figure.

solutions for the parameters. However, most poorly retrieved parameters still have their true values within the $1\,\sigma$ range of the
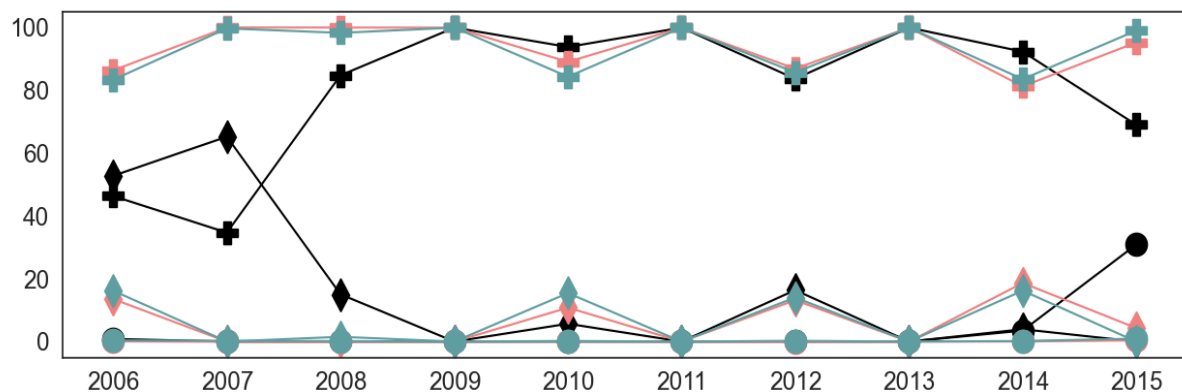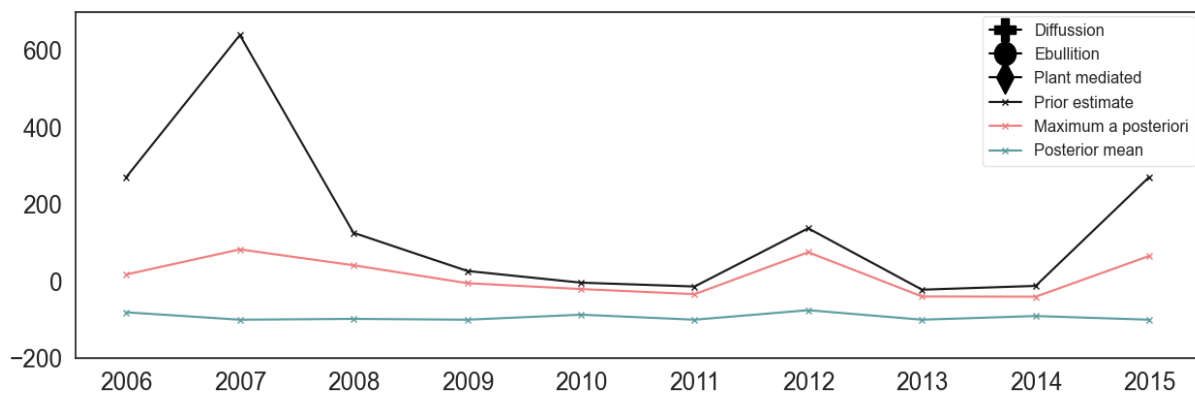
Figure 10. Flux component fractions and percentage model-data difference. Figure (a) shows the proportions of annual flux components plotted as a function of the total yearly flux. The different flux components are represented in solid lines of different colours, and the symbols on them correspond to each flux component. Figure (b) shows the annual model–observation mismatch in percentage with respect to the yearly total CH_4 observation.

Gaussian PDFs of the optimised values. Even when the parameters are slightly off from the Z_{true} values, Fig. 4 shows the
470   capability of the twin experiments in capturing the structure of the observations including the observed spikes in it.

The occasional lack of convergence mentioned above likely introduces a slight bias in the posterior estimates, i.e. compensating effects due to the equifinality in subsequent real data analyses, leading to suboptimal parameter estimates. This equifinality is essentially based on the high non-linearity of the model and a missing observational data constraint that would help distinguishing between certain parameter combinations. Nevertheless, in contrast to other similar studies, like Santaren et al. (2014),
475   which have encountered challenges in achieving complete recovery of many true parameter values, our GRaB-AM algorithm showed better performance in recovering true parameter values. The analysis of the cost function reduction (Table 4), the ability to constrain the parameters (Fig. 3), the ability to capture the structure of the model (Fig. 4), and the parameter retrieval ability
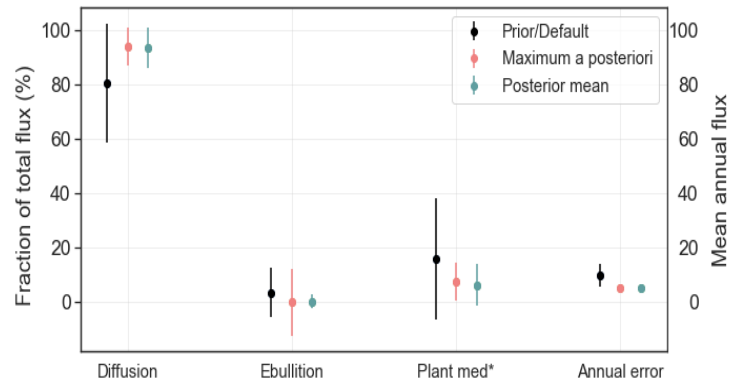
Figure 11. The first three columns of the figure show the fractions of the annual fluxes from process components of the total fluxes. The vertical solid lines represent the 1σ error bars of each component, and the dots represent the mean of the annual fluxes. The fourth column (correspond to y axis on the right side) shows the annual mean and annual errors for the inter-annual variation of the total fluxes.

of the twin experiments (Fig. 5) showed that the developed GRaB-AM algorithm is still capable of optimising the process parameters related to CH_4 emissions in LPJ-GUESS given the caveats mentioned above on the equifinality.

480   Similarly, the systematic low χ^2 values observed for the twin experiment doesn't necessarily affect the framework's ability to be set up for the real data experiment (Sect. 3.1). As the twin experiments here are under the assumption of an 'idealised model', meaning the model perfectly reproduces the observations without any errors or uncertainty, and 'error-free data', where the data perfectly represents the environmental conditions without any random errors, it is expected to have χ^2 values systematically below 1. Also, the χ^2 value is highly sensitive to the number of observations and parameters. Having 3,650

485   observations in scenario 1 and 41,610 observations in scenario 2, and only 11 parameters, can lead to low χ^2 values. However, the comparatively smaller values of χ^2 for sets 1 and 3 in scenario 1 and set 3 in scenario 2 indicates a tendency to over fitting the results and being overconfident in the estimated posterior values and uncertainties.

4.2   Parameter estimation using real observations

As described in Sect. 3.2.1 the experiment using real data resulted in three poorly constrained and one edge-hitting parameter.

490   The poorly constrained or edge-hitting parameters, however, are not uncommon in MH parameter search and rather expected with a complex and highly non-linear model such as LPJ-GUESS. The correlation of parameters to other parameters can affect the result; i. e. the number of parameters that can be optimised within this data assimilation framework is limited. Though the twin experiments showed good parameter retrieval capabilities, assimilating the real-world observations into a complex ecosystem model like LPJ-GUESS is expected to have parameter retrieval and equifinality problems. This is another reasons

495   for selecting a small subset of the parameters associated with wetland CH_4 flux simulations for this study. Considerable changes have occurred to the prior parameter values after optimisation. Here it should be considered that, in this study, the assimilation
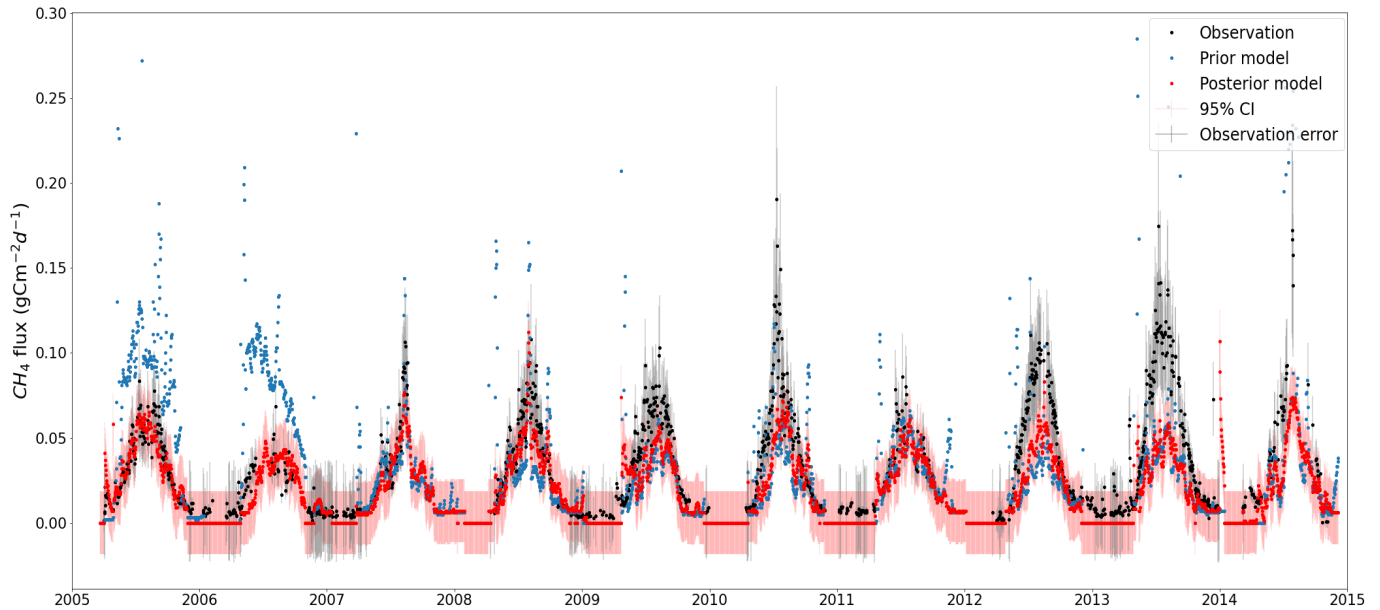
Figure 12. Total CH$_4$ simulation from the LPJ-GUESS model (red dots) after optimising with the GRaB-AM algorithm. The black dots are the real CH$_4$ observations from Siikaneva with prior observation error (grey shade). The light red shade around the posterior model simulation is the 95 % confidence interval (*CI*) of the simulations. The blue dots are the prior simulation with the prior default model parameters. A few outliers above 0.3 gCm^{-2} on the vertical axis have been removed from the figure for better visualisation. While most of the observations fall within the confidence intervals, it's important to note that the effects of parameter variations in the posterior are part of these confidence intervals.

aims to reduce the magnitude of the prior CH$_4$ flux simulation to minimise its misfit with the observed data, which is nearly half of the prior model estimate (see Table 6).

4.2.1 Posterior correlation estimates

500   The following discusses the possible impact of the posterior parameters (shown in Table 5) on CH$_4$ flux simulation, the interactions between the optimised parameters and the component fluxes shown in Fig. 8, as well as parameter-parameter correlations in Fig. 9 (we distinguishes between strong (> 0.5) and weak (< 0.2) parameter correlations; we focus on the strong ones here).

    The very slight reduction, i. e. , within 1/3 of the 1σ error observed in the posterior mean estimate of $Rmoist$ (Table 5). This indicates a slight decrease in the moisture response under aerobic conditions, which would likely result in a slower soil carbon 505   turnover time with a slight decrease in CH$_4$ emission. The weak R^2 value and the weak positive β value of $Rmoist$ with all the flux components indicate that a decrease in this parameter value decreases the emission and explains some of the variances in the flux components (Fig. 8).

    In contrast, $Rmoist_{an}$ obtained a higher posterior value compared to the prior (Table 5) with a slightly asymmetric multimodal distribution (see Fig. 7) indicating an increase in the moisture response in the anaerobic catotelm. Together with this,

510   the strong negative correlation (-0.8) observed between $Rmoist$ and $Rmoist_{an}$ (Fig. 9), indicates reduced decomposition in acrotelm and increased decomposition in catotelm. $Rmoist_{an}$ had a positive effect on diffusion and a negative effect on plant-mediated transport (Fig. 8). An increase in $Rmoist_{an}$ could enhance CH_4 production in the catotelm. Since catotelm has low plant root abundance, this increase would lead to more diffusion and a reduction in total plant-mediated transport. The increase in $Rmoist_{an}$ contributed very little to ebullition. This is most likely due to the negligible contribution of ebullition to the

515   overall flux, having zero contribution most of the time.

     The posterior CH_4/CO_2 parameter, which is the CH_4 to CO_2 ratio in an anaerobic environment, was found lower as compared to the prior (Table 5). This indicates a high fraction of CO_2 production from the peat compared to CH_4 production. The very high R^2 value of CH_4/CO_2 for diffusion and plant-mediated transport (which represent the two diffusive pathways) indicates that a significant portion of the variance in these pathways can be explained by this parameter (Fig. 8). Similarly, the

520   high, positive β value for diffusion and plant-mediated transport indicates a substantial linear increase in emissions through these pathways if the parameter is increased. The increase in ebullition is marginally less than the other fluxes, most likely because ebullition is limited by the availability of gaseous fraction of CH_4. The dissolved CH_4 will first emit via diffusive fluxes; hence, there could be very little CH_4 left in the gaseous phase for ebullition. The CH_4/CO_2 ratio is negatively correlated with the parameters $Rmoist_{an}$ and λ_{root} (Fig. 9). This indicates a lower CH_4 fraction produced by decomposition in deep soil.

525   The prior parameter value for f_{air} was zero, which means there is no 'permanent' gas fraction in peat (Table 5). The posterior value of f_{air} showed slightly positive (0.032), indicating a small air fraction in the peat. The f_{air} showed a very high positive correlation to por_{acro}, which can simply be explained as more porous soil allows for more air in the soil (Fig. 9). An increase in the f_{air} value would increase all the flux components, with a notably larger effect on diffusion (Fig. 8). As stated in Sect. 2.2.3, the diffusivity of CH_4 in air is four orders of magnitude greater than that in water, indicating that a higher fraction of

530   air in the soil results in the rapid and easy transport of CH_4 to the atmosphere. The larger increase in diffusion can be directly attributed to the f_{air} since this parameter directly controls diffusion.

     The fraction of available oxygen utilised for CH_4 oxidation is determined by the parameter f_{oxid}, which has a higher value after the optimisation (Table 5). The high values of f_{oxid} and f_{air}, indicating a high available air fraction, and hence, high O_2 concentration in the soil, result in the conversion of most of the available carbon into CO_2. This could explain the above

535   mentioned reduction in CH_4/CO_2 as a balancing effect (Eq. 2). The f_{oxid} showed a negative β value to diffusion and ebullition and a slight positive β value with comparatively high R^2 value to plant-mediated transport (Fig. 8). A decrease in ebullition can be explained by the increased availability of oxygen for CH_4 oxidation, resulting in less CH_4 being emitted via ebullition. A significant decrease occurs in diffusion because the diffusive flux cannot bypass the top layer, into which oxygen diffuses. Directly explaining the increase in plant-mediated transport is difficult due to the complex process formulation in the model.

540   However, it can be accounted that the aerenchymas could transport a part of the oxygen deep down to the soil layers where it plays less of a role in oxidation, but contributes more to the total gas pressure, which can escalate the passive plant mediated transport to the atmosphere.

     The optimisation of plant-related parameters depends on the specific plant species present in the wetland. A slight reduction in the posterior mean estimate of ϕ_{tiller} suggests that the tillers may be slightly more compact, with reduced porosity for

545 CH$_4$ transport. A considerable reduction, more than 1/3 of the prior uncertainty, is observed in w_{tiller}, indicating lower leaf biomass (Table 5). This reduction in potential leaf cover would lead to less carbon added to the 'potential carbon pool' for methanogens, resulting in lower CH$_4$ emissions. A decrease in tiller weight would add less organic carbon to the soil, leading to a less compact peat accumulation in the bottom soil layers with more porosity for water. This could explain the negative correlation between w_{tiller} and por_{cato} (Fig. 9). In contrast to the values of the two above-mentioned CH$_4$ transport-related

550 parameters, r_{tiller}, which represents the tiller radius of plants, showed a value more than twice the prior value (Table 5). This increase indicates more cross-sectional area of tiller for a given biomass, resulting in an increase in plant-mediated CH$_4$ transport (see Eq. 8). These three parameters related to plant-mediated transport showed strong positive correlation with each other. They also exhibited positive β values in relation to plant-mediated transport (Fig. 8). These parameters can have two effects on emissions. On the one hand, having aerenchyma cells with more porous space, radius, and biomass enhances CH$_4$

555 transport to the atmosphere. On the other hand, through the same spacious aerenchyma cells, it is also possible for plants to transport more O$_2$ to the soil. This enhanced O$_2$ transport to the soil could explain the slight reduction in diffusion and ebullition observed in the cases of ϕ_{tiller} and w_{tiller}.

The posterior value for the porosity in the catotelm (por_{cato}) was significantly lower than the prior (Table 5), suggesting a more compact catotelm with less water (as it is assumed to be saturated). This change could have a dual effect on CH$_4$.

560 Variations in water content can slightly affect soil temperature, potentially leading to an increase in the flux if the temperature rises, or a decrease in the flux due to the compact peat. As described in Sect. 3.2.1, por_{acro} remained unchanged, indicating no changes in acrotelm porosity (Table 5). The positive kurtosis observed in the PDF of this parameter indicates a well-constrained single solution, while the negative skewness indicates a more probabilistic region below the posterior estimate. Similar to f_{air}, por_{acro} also exhibited positive β values for all flux components, but with a relatively low R^2 value (Fig. 8).

565 This positive relationship may be attributed to the increased presence of air in the acrotelm soil, which could facilitate CH$_4$ emissions. In contrast, an increase in por_{cato} could lead to a slight reduction in ebullition. This could be because more water can potentially occupy the pores of permanently saturated catotelm which will indirectly affect ebullition through phase change and by affecting on soil temperature.

The posterior value for λ_{root} is estimated to be much smaller than the prior (higher than the value reported in Wania et al.

570 (2010) and in Susiluoto et al. (2018)), i. e. more than 1/3 of 1σ of the prior estimate (Table 5). This small posterior value for λ_{root} indicates a low decay length of root biomass in the soil, means more of the decomposition and CH$_4$ production occurs in the acrotelm, and less in the catotelm. The emission of CH$_4$ produced mainly by peat decomposition in the acrotelm would be facilitated by a low posterior value for λ_{root}, with around 60% in the first layer of acrotelm followed by 22% and 8% in the second and third layers of acrotelm. λ_{root} played a key role in this optimisation. Figure 8 shows that λ_{root} has a strong

575 negative β value for diffusion and a weak positive β value for plant-mediated transport, both with relatively strong R^2 values (Fig. 8). Since most of the peat decomposition activities are assumed to occur in the acrotelm, the reduction in the magnitude of λ_{root} could facilitate diffusion, especially as it is the largest component. On the other hand, plant-mediated transport may be reduced, as it limits the distribution of roots in soil depths.

4.2.2 Posterior flux components

In Fig. 13, the time series of process components is shown for the posterior mean estimate. In general, the optimisation of the model parameters leads to an approximately 50% decrease in the production of CH_4 compared to the prior, with a significant reduction in plant-mediated and ebullition components, leaving diffusion as the dominant component. Diffusion is reduced by around 30%, and plant-mediated transport is reduced by approximately 86%.

The low contribution of plant transport is mainly due to the reduced value of the root depth-controlling parameter λ_{root}, which decreased from 25.17 to 10.58. This smaller proportion of plant-mediated transport is somewhat surprising for a fen wetland site like Siikaneva, which features a significant aerenchymous leaf area throughout the growing season. The result is contradictory to the results obtained from optimising the HIMMELI model (Susiluoto et al., 2018), in which the largest fraction of CH_4 is contributed by the plant-mediated transport. However, field experiments conducted to estimate plant-mediated transport by Korrensalo et al. (2022) have observed a smaller proportion of the ecosystem-scale CH_4 flux attributable to plant CH_4 transport in the Siikaneva fen site. This observation aligns well with the results we obtained.

The largest reduction, however, was for ebullition by around 92 %. This result is not surprising since Wania et al. (2010), who provide the basic foundation of the CH_4 model in LPJ-GUESS, also reported almost virtually no ebullition to the surface at several sites. Figure 13 shows that during the years 2008, 2010 and 2012, no ebullition is estimated. Here, it should be considered that the representation of ebullition in LPJ-GUESS is somewhat simplified using a curve-fitting equation to calculate the solubility, and using the ideal gas law to convert the volume of CH_4 per volume of water into the corresponding number of moles. Due to this lack of detail and its fast timescale occurrence (mostly depends on the physical parameters such as temperature and pressure), and with no relevant parameters in the control vector, the optimisation could not alter the ebullition component directly. However, ebullition is indirectly controlled by parameters related to CH_4 production and transport when there is high saturated CH_4 available in the soil water. Thus, the optimisation can indirectly affect the ebullition. The total observed CH_4 flux from Siikaneva during the period of 2005 to 2014 was 56.0 gCm^{-2}, while the prior model estimate was 98.5 gCm^{-2} (Table 6). After the optimisation, with the posterior mean estimate of parameter values, the model estimated a flux of 53.5 gCm^{-2} with an estimated posterior uncertainty of $\mp$ 4.82 gCm^{-2}. This shows a reduced model-data error after optimisation with a difference of only 2.5 gCm^{-2}.

4.2.3 Posterior process-process correlation

After the optimisation, the air fraction in the peat got increased, which is likely the cause of the enhanced diffusion. Diffusion is estimated in the model based on the soil porosity, water, temperate and air fractions in the soil. Correlating the diffusion to the ebullition showed a negative result, i. e. illustrating the dominance of diffusion over ebullition (see Fig. 8b). A larger air fraction in the soil can also lead to an increase in plant-mediated emission as the passive diffusion of air through the plant tissues depends on the amount of air in the soil/peat water (see Sect. 2.2.3). This can be seen in Fig. 8b as a comparatively high correlation between diffusion and plant-mediated transport. The increased tiller radius r_{tiller} in plants increases the A_{tiller} value (Eq. 8), hence favours faster diffusion through the aerenchyma cells. Ebullition is positively correlated to plant-mediated
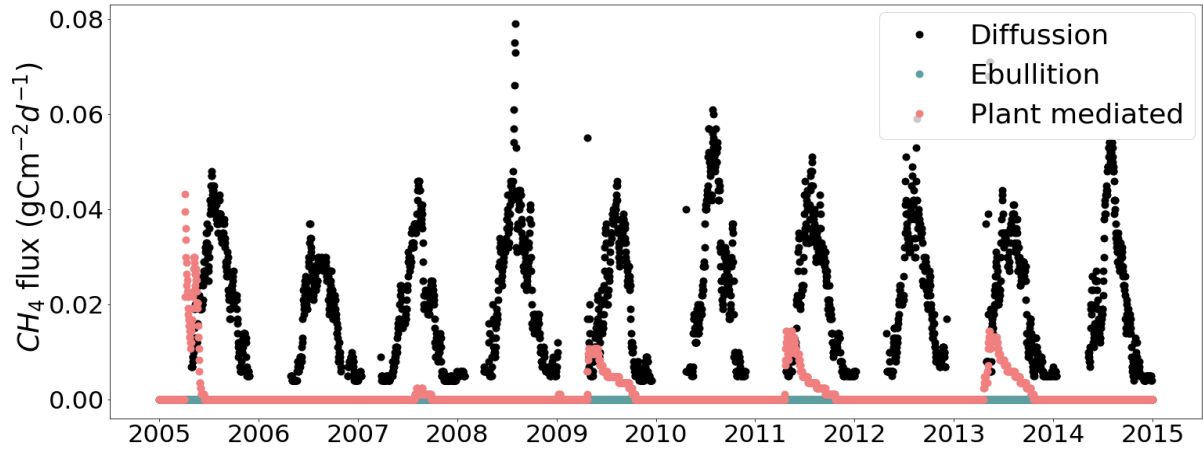
Figure 13. Time series for diffusion, ebullition, and plant transport using parameter values from the posterior mean estimate. A few outliers above 0.08 gCm^{-2} on the vertical axis have been removed from the figure for the better visualisation.

Table 6. Total emissions from flux components estimated from the MAP, posterior mean, and prior parameter values for all the ten years of the optimisation. The unit is in gCm^{-2}.

Component	MAP	Posterior mean	Prior	Observation
Diffusion	49.5	49.6	70.7	
Ebullition	0.15	0.28	4.1	
Plant-mediated	3.5	3.7	23.6	
Total	53	53.5	98.5	56.0

transport, indicating the occurrence of both these components when there is a high concentration of CH$_4$ in the soil. This occurs when the water table is located close to the surface and when there is a higher density of graminoids. An increase in plant-mediated transport of gases to the soil increases the net pressure imposed by the gases in soil/peat water, which could

615 also lead to increased ebullition.

4.3 Model error and fit to the observation

Except for ebullition, all the prior process components exhibited larger variances of the annual errors compared to the posterior estimates (Fig. 11). The plant-mediated transport is the component with the largest error in the prior estimate. The posterior error estimates for this component showed nearly equal values with a slightly higher value for the posterior mean estimate. A

620 similar pattern can also be seen for diffusion. In contrast to this, the MAP error estimate for ebullition showed a higher value compared to the posterior mean error but interestingly also to the prior. The posterior mean error estimate for ebullition showed the lowest value.

The annual sums of flux components mentioned above are illustrated in Fig. 10a. It is clear from this figure that the prior process components had large inter-annual variance, especially for the first three years and the last year. Considerable reduction in variance is observed for both the MAP and posterior mean estimates. The reduction of the variance observed in posterior estimates is not proportional to the prior, but still, the posterior estimates showed comparatively high variance in the first and last years. In Fig. 10b, as described in Sect. 3.2.4, the posterior mean estimate shows a comparatively high variance (w.r.t the MAP estimate) of the annual errors with a negative bias throughout the time period. In contrast to this, the MAP estimate showed a positive bias throughout the time period. Compared to the posterior mean estimate, the MAP estimate has considerably larger parameter values for the ϕ_{tiller} and r_{tiller} which could possibly be interpreted as slightly more CH_4 emission through the increased tillers of plants, hence the reason for the positive bias of the MAP estimate. Figure 11 also indicates a high percentage of annual plant-mediated emissions for the MAP estimate. The negative bias of the posterior mean estimate could be due to the additional wintertime emission from the real-world wetlands, which is not captured in the model. In the model, the emissions start around early summer, once the soil is not frozen anymore. In addition, the large daily variability in the observations of the summertime fluxes is also not represented in the model. Overall, the posterior estimates of the annual fluxes are in good agreement with the observations leading to a small model-data mismatch for both MAP and posterior mean estimates.

4.4 Model inputs and uncertainty

As mentioned in the Sect. 3.3, a somewhat pronounced systematic underestimation in emissions was observed in the years 2010, 2012, and 2013. None of the twin experiments exhibited these systematic errors, which indicates that the issue could be attributed to a structural model error (see Fig. 4). While the CH_4 module within LPJ-GUESS is relatively comprehensive when compared to many other similar models, the model's process description and parameterisation remain incomplete. For instance, in the real world, wind plays a crucial role in CH_4 emissions and its atmospheric concentration. However, in LPJ-GUESS, wind speed is set to zero for modelling convenience, which presents a significant limitation. Similarly, the lack of representation of air pressure, simplified representation of ebullition (see Sect. 4.2.2) and simplified representation of CH_4 production (see Eq. 2) are also a major limitation. Another reason for this mismatch could be the variations in the input climate data. The correlation plots of the input environmental variables of LPJ-GUESS and the CH_4 residuals (Supplement Fig. S3) indicate that, in these years, it showed a comparatively high correlation with swr and air temperature, though precipitation did not show any significant relation. The results of the sensitivity study indicate that both the prior and posterior model estimates are significantly sensitive to the input variables. However, the posterior model estimate exhibited a considerable reduction in sensitivity especially for swr and precipitation (see Sect. S5 and Fig. S5 in Supplement).

As mentioned in Wania et al. (2010), the flux components are determined by complex processes that depend on changes in many environmental factors. The model is unable to represent peak emissions caused by these micro-environmental changes. For instance, ebullition (one of the more complex CH_4 emissions processes in LPJ-GUESS, as explained in previous sections) depends on the volumetric content of wind and various gases, as well as hydrostatic and atmospheric pressure. However,

the model does not use them as forcing variables. Ebullition is also affected by the concentration of CH_4 and the density of nucleation sites, which are difficult to represent in the model.

It should be noted that the incomplete state vector used for optimisation might have affected the optimised model result. The process representations in LPJ-GUESS are complex and interconnected, with a multitude of parameters directly or indirectly linked to CH_4 fluxes. Representing the indirect parameters can be intricate, as they may depend on other fluxes or model components. For instance, LPJ-GUESS' soil module is intricately connected to the Century model, featuring ten soil compartments. Introducing a parameter related to soil temperature or the wtd into the framework would necessitate accounting for the intricacies of the Century model. Furthermore, it might require the inclusion of additional flux species, such as Net Primary Production (NPP), Soil temperature profiles, or wtd. This would significantly increase the complexity of the problem, exceeding the scope of this paper. Given these caveats, the small negative biases obtained for the posterior mean estimates when compared against the observations (see Fig. 10b) are reasonable considering the quality and uncertainty of the input data used (see Sect. 2.1) and the complexity and structural issues of LPJ-GUESS.

4.5 Optimised simulation from LPJ-GUESS

A detailed time series distribution of prior and posterior model simulations plotted against the observations is shown in Fig. 12. The posterior model predictions were adjusted by the optimisation to fit the observations with considerable adjustment to the summer peaks. For example, the large peaks in the modelled emissions in 2005 and 2006, which largely contributed to the prior cost function, disappeared in the posterior emissions. In the following years, 2007 and 2008, the prior model simulations underestimated the observation, which also got corrected in the posterior. Also, the posterior emissions largely capture the comparatively high peaks in the observations for the years 2010 and 2012, though the model still underestimated the observations. In 2013, the observations were high and the optimisation failed to capture this peak; rather, it tried to compensate for the underestimation by releasing a sudden high spike at the end of the summer that year. In winter months, the model simulated zero fluxes (as discussed before), whereas, the observations showed a small emission (around 8.3 % of the assimilated total), often with some small spikes possibly from the ebullition. This inability of the model to capture the wintertime emission has contributed to the posterior model uncertainty and model data misfit.

A significant mismatch in soil temperature and wtd has been observed between the model and observations, especially during the wintertime (see Sect. S4 and Fig. S4 in Supplement). The model tends to overestimate wintertime temperatures and underestimate the wintertime wtd, indicating completely frozen soil with a very low wtd. This discrepancy could be a reason for the complete suspension of model CH_4 emissions during the winter. Observations show many days with wtd above the ground level, both in summer and winter. Since wtd is a key factor that can affect all flux components, this error could contribute to the misfits observed after the optimisation, though it cannot explain the systematic under estimation observed in posterior. It should be noted that there are no considerable differences observed between the prior and posterior soil temperature or wtd.

As discussed in Sect. 4.2.3, the contribution of ebullition to the posterior estimate is comparatively negligible. Compared to the posterior, there were many emissions spikes observed in the prior estimate, especially during the beginning and the end of

the summer months. Apart from these spikes the prior CH_4 estimates during the summer were a bit low in most of the years. The posterior estimate has considerably reduced these high spikes and adjusted the summer peaks to match the observations better. On the other hand, while compromising with the summer peaks in the observations, the model with the optimised parameters often failed to capture the abrupt high fluxes in the daily observation and has simulated them at slightly wrong times. The spike shown at the end of 2013 is an example of such a mis-timing. This is likely to be caused by errors in the meteorological input data and missing wind and pressure representation.

It can be seen from the Fig. 12 that the majority of the observations lie within the 95 % confidence interval of the posterior estimate. Often the observation uncertainty overlaps the confidence interval except for the summer peak times of 2010, 2012 and 2013, in which the observations showed strong peaks compared to the average values. The few outliers in the observations are not captured by the model; these could likely be measurement artefacts and/or due to environmental forcing not considered here, again such as wind speed or air pressure.

4.6 Merits and shortcomings of GRaB-AM framework

Advantages of the developed GRaB-AM framework includes the ability of the MCMC method to escape local maxima or minima, making it more robust to these than gradient descent based methods. Further, the MCMC method is derivative free avoiding issues with computing gradients for very rough (non-continuous) functions. The adaptive part of the MCMC 'learns' about parameter correlations and utilises these dependencies in the proposal allowing it to better explore the parameter space. Potential issues for the MCMC is that very uneven cost functions can lead to the chain getting stuck (essentially the local minima is too deep for the algorithm to escape). Here, we have alleviated this issue by the tapering of the cost function. We also acknowledge that the cost function could be improved, the squared cost function essentially assumes Gaussian errors with equal variance for all values and ignores any temporal correlations. The observations are measured as time-series and concentration/flux observations are known to have spatio-temporal error correlations. Adapting the cost function to account for these factors would be of interest and is likely to have a larger impact on the posterior parameter uncertainties than on the estimates of the parameters.

In principle, the twin experiment should be able to recover all the parameters completely. However, the twin experiment in this study did not completely recover the true values of some parameters, especially the parameter CH_4/CO_2. This could be attributed to one or more of the following issues: 1) Due to the complex and extremely non-linear nature of LPJ-GUESS, there is a high possibility of equifinality. 2) The high dimensionality of the problem and limited variability in the data could be a reason for the poor convergence of some parameters. 3) The model is not fully constrained by the limited dimensions in both the data and the parameter space. Achieving complete convergence may require incorporating a) additional complementary observations capable of constraining additional model processes and b) additional parameters from different modules of the model that represent different model processes.

The failure observed in convergence is expected to yield suboptimal parameter estimates with too optimistic posterior uncertainty estimates due to the equifinality problems in the real data experiments. It may also be result in slightly corrupted relationships between variables, leading to changes in the covariance structure of the posterior parameters estimated from the

real data. Considering the high degree of non-linearity in the model, a single type of twin flux from a single site might not be sufficient for identifying all the parameters. Therefore, additional sites spanning a large climatic variability and/or different species of twin fluxes from the same site may be necessary. For instance, regarding the parameter CH_4/CO_2, one reason for the poor recovery could be that the study only optimises the CH_4 component, leaving the CO_2 fluxes significantly off. Incorporating both CH_4 and CO_2 fluxes to address both sides of the ratio can lead to a more accurate convergence. However, a challenge in this approach would involve formulating cost functions for different observations in a manner that properly weights them to equally represent the information without diminishing their significance. These considerations are beyond the scope of this paper.

5 Conclusions

This study represents an initial effort to optimise the model process parameters controlling the simulation of wetland CH_4 fluxes within the LPJ-GUESS model using the Rao-Blackwellised adaptive MCMC technique based on Bayesian statistics. The assimilation framework has been shown to be able to retrieve true parameter values within the uncertainty limits discussed above by performing a set of twin experiments. Further, we used eddy-covariance flux measurement data from a boreal wetland to calibrate the LPJ-GUESS model parameters for a site-specific simulation. The results demonstrated that the fit to the observation of the CH_4 simulation of a complex terrestrial DGVM like LPJ-GUESS can be systematically enhanced with a Bayesian parameter calibration. The results also showed that the modelled processes and the estimated parameters were well constrained by the observations leading to a substantial reduction in the posterior uncertainty of the simulated CH_4 emissions. However, we note here that due to the equifinality problems identified in the identical twin experiments, the posterior parameter values contain compensating effects caused by non-linearity of the model and lacking additional observational data constraint to uniquely identify each individual parameter. The results of the re-sampling experiment and the parameter and process correlations indicated that there were no redundant processes in the model description.

The robustness of the assimilation framework developed in this study calls for further application of the framework using observations from multiple sites in a simultaneous assimilation. Further validation of the framework's performance is necessary to confirm its applicability to other sites with diverse plant functional types and climatic conditions. The relatively strong roughness in the shape of the cost function observed in this study is expected to be reduced in a multi-site assimilation experiment, as has been observed by Kuppel et al. (2012), and which would provide additional observational data constraints to allow the retrieval of the global minimum of the cost function more easily and reduce the equifinality problem. These further applications are beyond the scope of this paper and will be investigated in future studies.

Code and data availability. The AMCMC code and CH_4 flux data used for this article are available at Data Depositions. The LPJ-GUESS model code can be obtained at LPJ-GUESS.

Author contributions. JTK designed the GRaB-AM assimilation framework with the help from MS and JL. PM developed the CH_4 model in LPJ-GUESS based on the work of Wania et al. (2010). MS and PM provided knowledge and advice about peatland CH_4 processes, and model parameters. JR and MR helped with collecting the CH_4 observation. MS and JL provided the supervision and technical advice with programming the algorithm and analysing results. JTK prepared the manuscript with contributions from all co-authors.

Competing interests. The authors have the following competing interests: At least one of the (co-)authors is a member of the editorial board of Geoscientific Model Development.

Acknowledgements. We thank Guillaume Monteil, Adrian Gustafson, Stefan Olin, and Johan Nord for the discussion of the computational setup and the manuscript. The Institute for Atmospheric and Earth System Research (SMEAR-INAR) at the University of Helsinki is acknowledged for the CH_4 flux data collected at Siikaneva. We would also like to acknowledge the Finnish Meteorological Institute (FMI), Finland, Research Council of Finland (336573, 341753, 325169) and ICOS-Finland for open data availability.

Financial support: This research has been partly supported by the Strategic Research Area: Biodiversity and Ecosystem services in a Changing Climate (BECC), Lund University, and is a contribution to the Strategic Research Area: ModElling the Regional and Global Earth system (MERGE). BECC and MERGE are funded by the Swedish government. It has also been partly supported by the Greenhouse Gas Fluxes and Earth System Feedbacks (GreenFeedBack) project from the European Union's Horizon Europe Framework Programme for Research and Innovation (project no. 101056921), funded by the European Union: "Views and opinions expressed are however those of the author(s) only and do not necessarily reflect those of the European Union. Neither the European Union nor the granting authority can be held responsible for them."

References

Aalto, J., Aalto, P., Keronen, P., Kolari, P., Rantala, P., Taipale, R., Kajos, M., Patokoski, J., Rinne, J., Ruuskanen, T., et al.: SMEAR II Hyytiälä forest meteorology, greenhouse gases, air quality and soil, https://doi.org/10.23729/23dd00b2-b9d7-467a-9cee-b4a122486039, university of Helsinki, Institute for Atmospheric and Earth System Research.

775 Ahti, T., Hämet-Ahti, L., and Jalas, J.: Vegetation zones and their sections in northwestern Europe, in: Annales Botanici Fennici, pp. 169–211, JSTOR, 1968.

Alekseychik, P., Kolari, P., Rinne, J., Haapanala, S., Laakso, H., Taipale, R., Matilainen, T., Salminen, T., Levula, J., Tuittila, E.-S., et al.: SMEAR II Siikaneva 1 wetland meteorology and soil, https://doi.org/10.23729/371cd3e4-26ae-41c9-96d7-69acccc206f7, university of Helsinki, Institute for Atmospheric and Earth System Research, a.

780 Alekseychik, P., Peltola, O., Li, X., Aurela, M., Hatakka, J., Pihlatie, M., Rinne, J., Haapanala, S., Laakso, H., Taipale, R., et al.: SMEAR II Siikaneva 1 wetland eddy covariance, https://doi.org/10.23729/bcc98726-ead8-45d4-ac39-1e4b1bf5e243, university of Helsinki, Institute for Atmospheric and Earth System Research, b.

Andrieu, C. and Thoms, J.: A tutorial on adaptive MCMC, Statistics and computing, 18, 343–373, 2008.

Aurela, M., Riutta, T., Laurila, T., Tuovinen, J.-P., Vesala, T., Tuittila, E.-S., Rinne, J., Haapanala, S., and Laine, J.: CO2 exchange of a sedge
785 fen in southern Finland-The impact of a drought period, Tellus B: Chemical and Physical Meteorology, 59, 826–837, 2007.

Aurela, M., Lohila, A., Tuovinen, J.-P., Hatakka, J., Riutta, T., and Laurila, T.: Carbon dioxide exchange on a northern boreal fen, 2009.

Bauer, L. and Hamby, D.: Relative sensitivities of existing and novel model parameters in atmospheric tritium dose estimates, Radiation protection dosimetry, 37, 253–260, 1991.

Bousquet, P., Ciais, P., Miller, J., Dlugokencky, E. J., Hauglustaine, D., Prigent, C., Van der Werf, G., Peylin, P., Brunke, E.-G., Carouge, C.,
790 et al.: Contribution of anthropogenic and natural sources to atmospheric methane variability, Nature, 443, 439–443, 2006.

Braswell, B. H., Sacks, W. J., Linder, E., and Schimel, D. S.: Estimating diurnal to annual ecosystem parameters by synthesis of a carbon flux model with eddy covariance net ecosystem exchange observations, Global Change Biology, 11, 335–355, 2005.

Bridgham, S. D., Pastor, J., Dewey, B., Weltzin, J. F., and Updegraff, K.: Rapid carbon response of peatlands to climate change, Ecology, 89, 3041–3048, 2008.

795 Broecker, W. S. and Peng, T.-H.: Gas exchange rates between air and sea, Tellus, 26, 21–35, 1974.

Carrassi, A., Bocquet, M., Bertino, L., and Evensen, G.: Data assimilation in the geosciences: An overview of methods, issues, and perspectives, Wiley Interdisciplinary Reviews: Climate Change, 9, e535, 2018.

Christensen, J. H., Hewitson, B., Busuioc, A., Chen, A., Gao, X., Held, I., Jones, R., Kolli, R. K., Kwon, W.-T., Laprise, R., et al.: Regional climate projections. Chapter 11, 2007.

800 Ciais, P., Sabine, C., Bala, G., Bopp, L., Brovkin, V., Canadell, J., Chhabra, A., DeFries, R., Galloway, J., Heimann, M., et al.: Carbon and other biogeochemical cycles. Climate change 2013: the physical science basis. Contribution of Working Group I to the Fifth Assessment Report of the Intergovernmental Panel on Climate Change, Comput. Geom, 18, 95–123, 2013.

Cronk, J. K. and Fennessy, M. S.: Wetland plants: biology and ecology, CRC press, 2016.

Dee, D. P.: Bias and data assimilation, Quarterly Journal of the Royal Meteorological Society: A journal of the atmospheric sciences, applied
805 meteorology and physical oceanography, 131, 3323–3343, 2005.

Dlugokencky, E.: NOAA/GML (gml. noaa. gov/ccgg/trends_ch4/), NOAA/GML, 2021.

Forster, P., Storelvmo, T., Armour, K., Collins, W., Dufresne, J.-L., Frame, D., Lunt, D., Mauritsen, T., Palmer, M., Watanabe, M., Wild, M., and Zhang, H.: The Earth's Energy Budget, Climate Feedbacks, and Climate Sensitivity, p. 923–1054, Cambridge University Press, Cambridge, United Kingdom and New York, NY, USA, https://doi.org/10.1017/9781009157896.009, 2021.

810 Gelman, A., Roberts, G., and Gilks, W.: Efficient Metropolis jumping rules, in: Bayesian Statistics 5, edited by Bernardo, J. M., Berger, J. O., Dawid, A. P., and Smith, A. F. M., pp. 599–607, Oxford University Press, 1996.

Ghil, M. and Malanotte-Rizzoli, P.: Data assimilation in meteorology and oceanography, in: Advances in geophysics, vol. 33, pp. 141–266, Elsevier, 1991.

Gustafson, A.: On the role of terrestrial ecosystems in a changing Arctic, Media-Tryck, Lund University, Sweden, 2022.

815 Hastings, W.: Monte Carlo sampling methods using Markov chains and their applications, Biometrika, 57, 97–109, 1970a.

Hastings, W. K.: Monte Carlo sampling methods using Markov chains and their applications, 1970b.

Hoffman, F. O. and Miller, C. W.: Uncertainties in environmental radiological assessment models and their implications, Tech. rep., Oak Ridge National Lab., 1983.

Jacob, D., Bärring, L., Christensen, O. B., Christensen, J. H., de Castro, M., Deque, M., Giorgi, F., Hagemann, S., Hirschi, M., Jones, R.,
820 et al.: An inter-comparison of regional climate models for Europe: model performance in present-day climate, Climatic change, 81, 31–52, 2007.

Jennison, C.: Discussion on the meeting on the Gibbs sampler and other Markov chain Monte Carlo methods, Journal of the Royal Statistical Society, Series B, 55, 54–56, 1993.

Johansson, T., Malmer, N., Crill, P. M., Friborg, T., Åkerman, J. H., Mastepanov, M., and Christensen, T. R.: Decadal vegetation changes in
825 a northern peatland, greenhouse gas fluxes and net radiative forcing, Global change biology, 12, 2352–2369, 2006.

Kirschke, S., Bousquet, P., Ciais, P., Saunois, M., Canadell, J. G., Dlugokencky, E. J., Bergamaschi, P., Bergmann, D., Blake, D. R., Bruhwiler, L., et al.: Three decades of global methane sources and sinks, Nature geoscience, 6, 813–823, 2013.

Korrensalo, A., Männistö, E., Alekseychik, P., Mammarella, I., Rinne, J., Vesala, T., and Tuittila, E.-S.: Small spatial variability in methane emission measured from a wet patterned boreal bog, Biogeosciences, 15, 1749–1761, 2018.

830 Korrensalo, A., Mammarella, I., Alekseychik, P., Vesala, T., and Tuittila, E.: Plant mediated methane efflux from a boreal peatland complex, Plant and Soil, 471, 375–392, 2022.

Kuppel, S., Peylin, P., Chevallier, F., Bacour, C., Maignan, F., and Richardson, A.: Constraining a global ecosystem model with multi-site eddy-covariance data, Biogeosciences, 9, 3757–3776, 2012.

Lerman, A. et al.: Geochemical processes. Water and sediment environments., John Wiley and Sons, Inc., 1979.

835 Mathijssen, P. J., Väliranta, M., Korrensalo, A., Alekseychik, P., Vesala, T., Rinne, J., and Tuittila, E.-S.: Reconstruction of Holocene carbon dynamics in a large boreal peatland complex, southern Finland, Quaternary Science Reviews, 142, 1–15, 2016.

McGuire, A., Sitch, S., Clein, J. S., Dargaville, R., Esser, G., Foley, J., Heimann, M., Joos, F., Kaplan, J., Kicklighter, D., et al.: Carbon balance of the terrestrial biosphere in the twentieth century: Analyses of CO2, climate and land use effects with four process-based ecosystem models, Global biogeochemical cycles, 15, 183–206, 2001.

840 McGuire, A., Christensen, T., Hayes, D., Heroult, A., Euskirchen, E., Kimball, J., Koven, C., Lafleur, P., Miller, P., Oechel, W., et al.: An assessment of the carbon balance of Arctic tundra: comparisons among observations, process models, and atmospheric inversions, Biogeosciences, 9, 3185–3204, 2012.

Metropolis, N., Rosenbluth, A., Rosenbluth, M., Teller, A., and Teller, E.: Equations of state calculations by fast computing machines, Journal of Chemical Physics, 21, 1087–1092, 1953a.

Metropolis, N., Rosenbluth, A. W., Rosenbluth, M. N., Teller, A. H., and Teller, E.: Equation of state calculations by fast computing machines, The journal of chemical physics, 21, 1087–1092, 1953b.

Millington, R. and Quirk, J.: Permeability of porous solids, Transactions of the Faraday Society, 57, 1200–1207, 1961.

Rinne, J., Riutta, T., Pihlatie, M., Aurela, M., Haapanala, S., Tuovinen, J.-P., Tuittila, E.-S., and Vesala, T.: Annual cycle of methane emission from a boreal fen measured by the eddy covariance technique, Tellus B: Chemical and Physical Meteorology, 59, 449–457, 2007.

Rinne, J., Tuittila, E.-S., Peltola, O., Li, X., Raivonen, M., Alekseychik, P., Haapanala, S., Pihlatie, M., Aurela, M., Mammarella, I., et al.: Temporal variation of ecosystem scale methane emission from a boreal fen in relation to temperature, water table position, and carbon dioxide fluxes, Global Biogeochemical Cycles, 32, 1087–1106, 2018.

Roberts, G., Gelman, A., and Gilks, W.: Weak convergence and optimal scaling of random walk Metropolis algorithms, The Annals of Probability, 7, 110–120, 1997.

Santaren, D., Peylin, P., Bacour, C., Ciais, P., and Longdoz, B.: Ecosystem model optimization using in situ flux observations: benefit of Monte Carlo versus variational schemes and analyses of the year-to-year model performances, Biogeosciences, 11, 7137–7158, 2014.

Saunois, M., Jackson, R., Bousquet, P., Poulter, B., and Canadell, J.: The growing role of methane in anthropogenic climate change, Environmental Research Letters, 11, 120 207, 2016.

Saunois, M., Stavert, A. R., Poulter, B., Bousquet, P., Canadell, J. G., Jackson, R. B., Raymond, P. A., Dlugokencky, E. J., Houweling, S., Patra, P. K., et al.: The global methane budget 2000–2017, Earth System Science Data, 12, 1561–1623, 2020.

Segers, R.: Methane production and methane consumption: a review of processes underlying wetland methane fluxes, Biogeochemistry, 41, 23–51, 1998.

Sitch, S., Smith, B., Prentice, I. C., Arneth, A., Bondeau, A., Cramer, W., Kaplan, J. O., Levis, S., Lucht, W., Sykes, M. T., et al.: Evaluation of ecosystem dynamics, plant geography and terrestrial carbon cycling in the LPJ dynamic global vegetation model, Global change biology, 9, 161–185, 2003.

Smith, B.: LPJ-GUESS-an ecosystem modelling framework, Department of Physical Geography and Ecosystems Analysis, INES, Sölvegatan, 12, 22 362, 2001.

Smith, B., Wårlind, D., Arneth, A., Hickler, T., Leadley, P., Siltberg, J., and Zaehle, S.: Implications of incorporating N cycling and N limitations on primary production in an individual-based dynamic vegetation model, Biogeosciences, 11, 2027–2054, 2014.

Susiluoto, J., Raivonen, M., Backman, L., Laine, M., Makela, J., Peltola, O., Vesala, T., and Aalto, T.: Calibrating the sqHIMMELI v1. 0 wetland methane emission model with hierarchical modeling and adaptive MCMC, Geoscientific Model Development, 11, 1199–1228, 2018.

Tang, J., Miller, P. A., Persson, A., Olefeldt, D., Pilesjö, P., Heliasz, M., Jackowicz-Korczynski, M., Yang, Z., Smith, B., Callaghan, T. V., et al.: Carbon budget estimation of a subarctic catchment using a dynamic ecosystem model at high spatial resolution, Biogeosciences, 12, 2791–2808, 2015.

Tarantola, A.: Inversion of travel times and seismic waveforms, Seismic tomography, pp. 135–157, 1987.

Wania, R., Ross, I., and Prentice, I. C.: Integrating peatlands and permafrost into a dynamic global vegetation model: 1. Evaluation and sensitivity of physical land surface processes, Global Biogeochemical Cycles, 23, 2009a.

Wania, R., Ross, I., and Prentice, I.: Implementation and evaluation of a new methane model within a dynamic global vegetation model: LPJ-WHyMe v1. 3.1, Geoscientific Model Development, 3, 565–584, 2010.

Wania, R., Melton, J., Hodson, E. L., Poulter, B., Ringeval, B., Spahni, R., Bohn, T., Avis, C., Chen, G., Eliseev, A. V., et al.: Present state of global wetland extent and wetland methane modelling: methodology of a model inter-comparison project (WETCHIMP), Geoscientific Model Development, 6, 617–641, 2013.

Wramneby, A., Smith, B., Zaehle, S., and Sykes, M. T.: Parameter uncertainties in the modelling of vegetation dynamics—effects on tree community structure and ecosystem functioning in European forest biomes, Ecological Modelling, 216, 277–290, 2008.

Zhang, W., Miller, P. A., Smith, B., Wania, R., Koenigk, T., and Döscher, R.: Tundra shrubification and tree-line advance amplify arctic climate warming: results from an individual-based dynamic vegetation model, Environmental Research Letters, 8, 034 023, 2013.

Zhang, Z., Zimmermann, N. E., Stenke, A., Li, X., Hodson, E. L., Zhu, G., Huang, C., and Poulter, B.: Emerging role of wetland methane emissions in driving 21st century climate change, Proceedings of the National Academy of Sciences, 114, 9647–9652, 2017.

885